IEEE Access
Multidisciplinary : Rapid Review : Open Access Journal

Received 12 March 2024, accepted 16 April 2024, date of publication 19 April 2024, date of current version 7 May 2024.

Digital Object Identifier 10.1109/ACCESS.2024.3391611

RESEARCH ARTICLE

Optimal α-Variable Model-Free Adaptive Barrier Function Fractional Order Nonlinear Sliding Mode Control for Four Area Interconnected Hybrid Power System With Nonlinearities

OMER ABBAKER AHMED MOHAMMED[1], LINGXI PENG[1], GEHAD ABDULLAH AMRAN[2], HUSSAIN ALSALMAN[3], MODAWY ADAM ALI ABDALLA[4], (Member, IEEE), OMAR ALKAWMANI[5], MUHAMMAD MURSIL[6], AND BASSIOUNY SALEH[7,8]

[1]School of Mechanical and Electrical Engineering, Guangzhou University, Guangzhou 510006, China
[2]Department of Management Science and Engineering, Dalian University of Technology, Dalian 116024, China
[3]Department of Computer Science, College of Computer and Information Sciences, King Saud University, Riyadh 11543, Saudi Arabia
[4]College of Energy and Electrical Engineering, Hohai University, Nanjing 211100, China
[5]College of Electronic Information and Telecommunication Engineering, Northeastern University, Shenyang 110169, China
[6]Department of Computer Engineering and Mathematics, University of Rovira i Virgili, 43002 Tarragona, Spain
[7]College of Energy and Power Engineering, Nanjing University of Aeronautics and Astronautics, Nanjing 210016, China
[8]Production Engineering Department, Alexandria University, Alexandria 21544, Egypt

Corresponding authors: Lingxi Peng (manplx@163.com) and Gehad Abdullah Amran (jehad.westran@gmail.com)

This work was supported in part by the Researchers Supporting Project, King Saud University, Riyadh, Saudi Arabia, under Grant RSP2024R244; and in part by the Tertiary Education Scientific Research Project of Guangzhou Municipal Education Bureau under Grant 202235165.

ABSTRACT This paper proposes an optimal α-variable model-free adaptive barrier-function fractional-order nonlinear sliding mode control ($\alpha(t)$-MF-ABFFONSMC) for the load frequency control (LFC) problem of a four-area interconnected hybrid power system with boiler dynamics and physical constraints. The proposed $\alpha(t)$-MF-ABFFONSMC is comprised of the ultra-local model (ULM)-based sliding mode disturbance observer (SMDO), proportional-differential (PD) controller, and adaptive barrier-function fractional-order nonlinear sliding mode control (ABFFONSMC). The ULM mechanism is utilized to re-formulate the complex four-area interconnected hybrid power system so as to reduce the controller's design complexity, wherein SMDO is utilized to observe and eliminate the uncertain dynamics or lumped disturbance. Then, the SMDO based-iPD controller is designed. However, there always exists non-null estimation error under the SMDO method and the control performance cannot be ensured. Therefore, the ABFFONSMC is proposed and inserted into the SMDO-iPD controller to avoid the impact of estimation error and improve the control performance. In addition, an adaptive gain based on barrier function is formulated to approximate the upper bound of SMDO's estimation error and thus decrease the undesired chattering on the sliding surface. Correspondingly, the $\alpha(t)$-MF-ABFFONSMC is established. Moreover, the parameter optimizer based on the Marine Predator Algorithm (MPA) is proposed to tune the parameters of the proposed $\alpha(t)$-MF-ABFFONSMC controller. Furthermore, using the Lyapunov theorem, the stability of $\alpha(t)$-MF-ABFFONSMC via a closed-loop system is verified. To validate the performance of the proposed controller, the numerical simulation on a four-area interconnected hybrid power system is carried out in a Matlab/Simulink environment. The corresponding simulation results are presented to show the superiority and effectiveness of the proposed technique.

INDEX TERMS Load frequency control, ultra-local model, adaptive barrier-function, nonlinear sliding mode control, sensitivity analysis.

I. INTRODUCTION

Electrical power plants are typically composed of various power plant units, such as thermal, gas, hydraulic,

The associate editor coordinating the review of this manuscript and approving it for publication was Ruisheng Diao.

nuclear, and renewable energy power plants. These units are effectively interconnected through the use of transmission lines, commonly referred to as tie-lines, which facilitate the coordination of many control areas [1], [2]. Any undesired discrepancy between generation and load demand resulting from load perturbations, unexpected disturbances, parameter uncertainties, and model uncertainties can lead to frequency deviation and interchange tie-line power flow from their scheduled limits. This problem brings out an aspiration to develop a precise and effective control mechanism in power system modeling known as load frequency control (LFC) [3], [4]. The main function of LFC in multi-area interconnected power systems is to maintain system performance measurements, such as area frequency and interchange tie-line power, at their designated values [5]. Therefore, it is necessary to implement a control strategy that not only achieves frequency stabilization and maintains the output power but also obtains zero steady-state error and prevents unintended scheduled power exchange.

On these aspects of stability, efficiency, and reliability of the interconnected power system, different control strategies have been developed for the LFC problem in recent years. Among them, fuzzy logic controller [3], [6], robust controller [7], intelligent-based adaptive controller [8], sliding mode controller (SMC) [4], [9], decentralized controller [10], and model predictive control [11] have been constructed to address the LFC problem. On the other hand, traditional approaches such as the PID controller and its different extended structures with heuristic methods have been widely studied as supplementary controllers for the LFC problem in the literature due to their simplicity and ease of design structure. In this regard, a tuned proportional integral (PI) controller based on RIME algorithm [12], an improved whale optimization algorithm based-PIDF-(1+PI) cascade automatic generation control [13], proportional integral derivative plus second order derivative (PID+DD) based-ant lion optimizer (ALO) algorithm [14], fractional order PID based-improved particle swarm optimization (IPSO) [15], fractional-order set-point weighted PID (FOSWPID) based on the hybridization of the fusion of flower pollinated algorithm (FPA) and pathfinder algorithm (PFA) (hFPAPFA) [16], cascaded fractional order tilt-integral-tilt-derivative (TI-TD) based on the mayfly algorithm [17], cascaded fractional order PI-fractional order PD based-dragonfly search algorithm (DSA) [18], three-degree-of-freedom fractional-order PID and fractional-order PI (3DOF-FOPID-FOPI) controller based on particle swarm optimization (PSO) and gravitational search algorithm (GSA) [19], have been successfully applied to achieve the control objectives in LFC problem. Though the aforementioned techniques made a significant contribution to the development of the LFC strategy, the increase in the complexity and size of power systems has necessitated the construction of new hybrid frameworks and the application of innovative methods in multi-area interconnected power systems. In [20], a fuzzy based-tilt-integral-derivative (TID) controller are proposed for renewable energy source integrated multi-area power system using a novel artificial hummingbirds' algorithm. In [21], a fuzzy PID structure based on a new intelligent genetic algorithm (GA) is developed to handle the LFC problem of a two-area thermal power plant. Similar to [22], the authors proposed an improved grey wolf optimization (IGWO) technique to tune the parameters of a fuzzy-aided PID controller for two area-interconnected power systems. Moreover, in [23], the authors presented a bee optimization algorithm to regulate the optimum parameters of the PID-fuzzy controller for a complex multi-area-interconnected power system.

Recent studies have confirmed that the utilization of the SMC technique is a proper strategy for effectively addressing uncertainty in a controlled system [24], [25]. The main advantage of SMC is that the controlled system demonstrates robustness characteristics concerning both external and internal perturbation, even without prior knowledge of the system dynamics [26]. Furthermore, SMC presents a methodical resolution that effectively addresses significant obstacles encountered in the engineering domain, including rapid transient response, noteworthy transient performance, and simple design for both linear and nonlinear systems. Therefore, a discrete-time SMC is proposed for the LFC of a four-area interconnected power system with nonlinearities to enhance the plant performance [4]. In [27], an optimal SMC is developed for the LFC of the two-area interconnected power system to reduce the frequency fluctuations. Moreover, in Ref. [28], the authors proposed an SMC-based optimization algorithm for interconnected two-area multi-source power systems, wherein the teaching learning-based optimization (TLBO) technique is used to tune the controller gains. Though many researchers neglected the effects of boiler dynamics and physical restrictions in the majority of LFC studies in the literature, these factors should be taken into account in the model in order to better capture the dynamics of the real system.

Fortunately, the ultra-local model (ULM) algorithm-based model-free control (MFC) has attracted tremendous attention from academics and is widely utilized in many control applications [8], [29], which decreases the reliance on model knowledge and depends merely on input and output information if compared to the model-based control strategies. The MFC's robustness mainly depends on the proposed estimator's ability to observe unknown, uncertain system dynamics, such as time-delay estimation (TDE) [30] and algebraic observer (AO) [31]. However, due to time delays and time windows, respectively, both the TDE and AO inevitably have approximation errors. Additionally, MFC based on extended state observers (ESOs) is developed [8], [33]. The ESO can only achieve asymptotic observation when the time derivative of the unknown, uncertain dynamics reaches zero; the estimation error will converge to zero as time tends to infinity. Therefore, the zero estimation error and finite-time observation of uncertain system dynamics are not considered in the aforementioned approaches.

In consideration of the aforementioned previous studies and discussions, this paper proposes an optimal α-variable model-free adaptive barrier-function fractional-order nonlinear sliding mode control ($\alpha(t)$-MF-ABFFONSMC) for LFC of four-area interconnected hybrid power systems incorporated with nonlinearities using a marine predators algorithm (MPA)-based parameter optimizer. The proposed $\alpha(t)$-MF-ABFFONSMC controller is constructed and applied to the plant model in the presence of nonliearities such as boiler dynamics, governor deadband (GDB), and generation rate constraint (GRC), and because disregarding these factors will cause unrealistic results for the controlled system. Furthermore, the superiority of the proposed method is evaluated via a comparative study with other methods such as the IPSO-optimized fractional-order PID controller (FOPID) [15], the SMDO-based intelligent PD controller (SMDO-iPD), the ALO-optimized PID+DD [14], the IGWO-optimized fuzzy PID controller [22], and hFPAPFA-optimized FOSW-PID [16]. Thus, the main innovations and novelties of this article can be summarized as follows:

1) It is the first attempt to propose an $\alpha(t)$-MF-ABFFONSMC strategy for addressing the LFC problem in four-area interconnected hybrid power systems incorporated with nonlinearities.
2) To avoid precise modeling information and decrease the difficulty of controller design, the ULM algorithm-based MPC is employed to re-formulate the complex nonlinear four-area interconnected hybrid power system. Unlike the existing ULM algorithm-based MFCs, the TDE [30] and AO [31] have unavoidable estimation errors due to the time delays and time windows, respectively. Furthermore, when the time derivative of the uncertain dynamics can not converge to zero, the ESO [8], [33] can only achieve bounded observation asymptotically. Therefore, in this paper, the SMDO is proposed to estimate the unknown, uncertain system dynamics, guaranteeing that the estimation error can converge to zero in a finite time.
3) Unlike [31] and [32], which assumed that the upper bound on the estimation error is known, this study considers that the upper bound on the estimation error is unknown. Thus, an adaptive parameter based on the barrier function is proposed to approximate it.
4) In the existing ULM algorithm-based MFCs [8], [30], [31], [32], [33], the value of α is fixed and pre-defined. In [34], an adaptive method based on a least-squares algorithm is presented to tune α automatically. Unlike [34], a new α-variable law is proposed to adjust the value of control gain automatically, aiming to enhance the tracking accuracy of the MFC.
5) The Marine Predators Algorithm (MPA) is proposed as a parameter optimizer to tune the gains of the proposed $\alpha(t)$-MF-ABFFONSMC strategy.
6) The stability of the proposed $\alpha(t)$-MF-ABFFONSMC approach is analyzed completely by using the Lyapunov approach, and the model of a four-area interconnected hybrid power system with the proposed method is realized in the Matlab/Simulink environment. Moreover, operating load perturbation, parameter uncertainties, and nonlinearities such as boiler dynamics and physical constraints are considered in the simulation to verify the robustness and efficiency of the proposed technique.

The rest of this paper is organized as follows: Preliminaries and dynamic modeling are presented in Section II. Then, the proposed controller strategy, stability analysis, and optimization technique are demonstrated in Section III. Next, the simulation results and discussion are presented in Section IV. Finally, the conclusion is made at the end of this paper in Section V.

II. PRELIMINARIES AND SYSTEM DESCRIPTION AND MODELLING

A. PRELIMINARIES

The definition of the fractional order can be represented by the general operator structures ${}_{t_0}D_t^{\gamma}$ and ${}_{t_0}I_t^{\gamma}$, which represent a generalization of the differential and integral operators, respectively [35].

Definition 1: The derivative of the function $x(t)$ with fractional order γ-based Riemann-Liouville can be given as [35]:

$$\begin{aligned} {}_{t_0}D_t^{\gamma} z(t) &= \frac{d^{\gamma} z(t)}{dt^{\gamma}} \\ &= \frac{1}{\Gamma(n-\gamma)} \frac{d^n}{dt^n} \int_{t_0}^{t} (t-s)^{n-\gamma-1} z(s) ds \end{aligned} \tag{1}$$

where t_0 is the initial time, and n is the first integer larger than γ, i.e., $n-1 \le \gamma < n$.

The integration of function $z(t)$ with fractional order γ based on Riemann-Liouville can be given as [35]:

$${}_{t_0}I_t^{\gamma} z(t) = \frac{1}{\Gamma(\gamma)} \int_{t_0}^{t} (t-s)^{\gamma-1} z(s) ds \tag{2}$$

where $\gamma \in \mathbf{R}^{+}$ and $\Gamma(\cdot)$ indicates for Euler's Gamma function.

Property 1: If n is an integer, there exists

$$\frac{d^n}{dt^n}\left[{}_{t_0}D_t^{\gamma} z(t)\right] = {}_{t_0}D_t^{n+\gamma} z(t) \tag{3}$$

Thus, the following notations can be utilised for convenience: (i) ${}_{t_0}D_t^{\gamma} z(t) = D^{\gamma} z(t)$ (ii) $\frac{dz(t)}{dt} = \dot{z}(t)$.

Lemma 1: [44] Consider the Lyapunov function $V(t)$ with an initial value $V(0)$ such that the following inequality holds:

$$\dot{V}(t) \le -mV^{d}(t), \quad \forall t \ge 0, \quad V(t_0) \ge 0 \tag{4}$$

where $0 < d < 1$ and $m > 0$. Then, the finite time t_f can be given as follows:

$$t_{\mathrm{f}} \le t_0 + \frac{V^{1-d}(t_0)}{m(1-d)} \tag{5}$$

Lemma 2: [44] Assume that the continuous and continuous positive-definite $V(t)$ satisfy the differential inequality for $t \geq t_0$ and $V(t_0) \geq 0$ as follows:

$$\dot{V}(t) \leq -cV(t) - mV^d(t), \quad \forall t \geq 0, \quad V(t_0) \geq 0 \tag{6}$$

where $c, m > 0$ and $0 < d < 1$. Then, the functional V(t) will converge to the origin in finite time t_f as follows:

$$t_f \leq t_0 + \frac{1}{c(1-d)} ln \frac{V^{1-d}(t_0) + m}{m} \tag{7}$$

B. SYSTEM DESCRIPTION AND MODELLING

Typically, a multi-area interconnected hybrid power system consists of multiple control areas, with each region networked to another through tie-lines, as displayed in Fig. 1. These tie-lines facilitate power exchange throughout the areas during normal operating conditions, thereby addressing any disparities between power generation and demand. Nevertheless, it is important to note that any disturbance in load within a given region has the potential to induce frequency oscillations throughout all control areas. Therefore, each designed control area should satisfy the following control objectives:

- To guarantee that the load frequency deviation oscillates in a relatively small zone around zero.
- To guarantee that the tie-lines's switching power flow returns to the pre-determined levels.

In this article, a nonlinear four-area interconnected hybrid power system that consists of reheat thermal mode [14], [15], [21] and wind turbine mode [36], [37] for all areas is considered, as shown in Fig. 1. Each area of an interconnected hybrid power system has LFC, and the reheat thermal power system in all zones is integrated with boiler dynamics and physical constraints such as GRC and GDB.

1) REHEAT THERMAL MODEL-BASED LFC

A detailed synthesis of a thermal system without a wind turbine model is presented in Fig. 2. Therefore, the mathematical expression of the system can be directly derived from the model, as shown in Fig. 2.

The dynamic model of the frequency deviation (Δf_i) and incremental mismatch power ($\Delta P_{tie,i}$, $\Delta P_{g,i}$, $\Delta P_{L,i}$) can be described as

$$\Delta \dot{f_i} = \frac{1}{T_{p,i}} \Delta f_i - \frac{K_{p,i}}{T_{p,i}} \Delta P_{tie,i} + \frac{K_{p,i}}{T_{p,i}} \Delta P_{g,i} - \frac{K_{p,i}}{T_{p,i}} \Delta P_{L,i} \tag{8}$$

where Δf_i represents the frequency error (Hz); $\Delta P_{g,i}$, $\Delta P_{tie,i}$, and $\Delta P_{L,i}$ denote the generator output power error (p.u. MW); the load perturbation (p.u. MW); and the tie-line power flow deviation (p.u. MW), respectively. $K_{p,i}$ and $T_{p,i}$ stand for the power system gain (Hz/p.u. MW) and the power system time constant (s), respectively.

The mathematical expression of the turbine unit model can be described as follows:

$$\Delta \dot{P}_{g,i} = \frac{1}{T_{t,i}} \Delta P_{g,i} + \frac{1}{T_{t,i}} \Delta P_{r,i} \tag{9}$$

where $T_{t,i}$ represents the time constant of the reheat turbine (s).

The speed governing system model can be expressed as follows:

$$\Delta \dot{X}_{g,i} = \frac{1}{T_{g,i} R_i} \Delta f_i + \frac{1}{T_{g,i}} \Delta X_{g,i} + \frac{1}{T_{g,i}} \Delta P_{c,i} \tag{10}$$

where $\Delta X_{g,i}$ and $\Delta P_{c,i}$ are the governor valve position deviation (p.u.) and the control signal, respectively. R_i represents the speed drop due to governor action (Hz/p.u. MW), and $T_{g,i}$ denotes the time constant of the thermal governor (s).

The following equation explains the mathematical expression of the reheat time delay system model as:

$$\Delta \dot{P}_{r,i} = -\frac{T_{r,i}}{T_{g,i} R_i} \Delta f_i + \left(\frac{1}{T_{r,i}} - \frac{T_{r,i}}{T_{g,i}} \right) \Delta X_{g,i} - \frac{1}{T_{r,i}} \Delta P_{r,i} \tag{11}$$

The deviation of tie-line power between areas i and j can be described as follows:

$$\Delta \dot{P}_{tie,ij} = 2\pi T_{ij} (\Delta f_i - \Delta f_j), \qquad \Delta \dot{P}_{tie,ij} = -\Delta \dot{P}_{tie,ji} \tag{12}$$

where T_{ij} denotes the interconnection gain between control areas (p.u. MW). The total interchange tie-line power between zone i and the other zones is calculated as follows:

$$\Delta \dot{P}_{tie,i} = \sum_{\substack{j=1 \\ j \neq i}}^{4} \Delta P_{tie,ij} = 2\pi T_{ij} \sum_{\substack{j=1 \\ j \neq i}}^{4} (\Delta f_i - \Delta f_j) \tag{13}$$

It is noted from above Eq. (13) that the control area $-i$ (for $i = 1, 2,3,4$) is interconnected with the control area j ($j \neq i$). The area control error (ACE), which is the input signal to the supplementary controller in LFC, is expressed as a linear combination of tie-line power and frequency errors for each area as follows:

$$ACE_i = B_i \Delta f_j + \Delta P_{tie,i} \tag{14}$$

where B_i denotes the frequency bias factor(p.u. MW/Hz).

2) GOVERNOR DEAD BAND (GDB)

The previous studies reported that the GDB can greatly affect the performance of a controlled system in a realistic power system [38]. According to [6], it is determined that one of the consequences of GDB is to boost the speed regulation of the steady state. These are some descriptions of the GDB nonlinearity in a real plant. An appropriate representation of the hysteresis type of nonlinearities can be expressed as follows [6]:

$$y = G(z, \dot{z}) \tag{15}$$

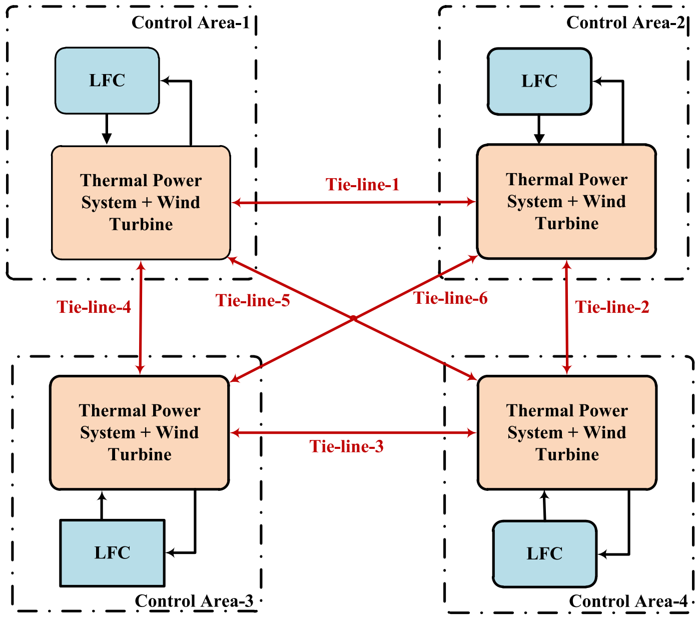

FIGURE 1. Four area interconnected electrical power system.

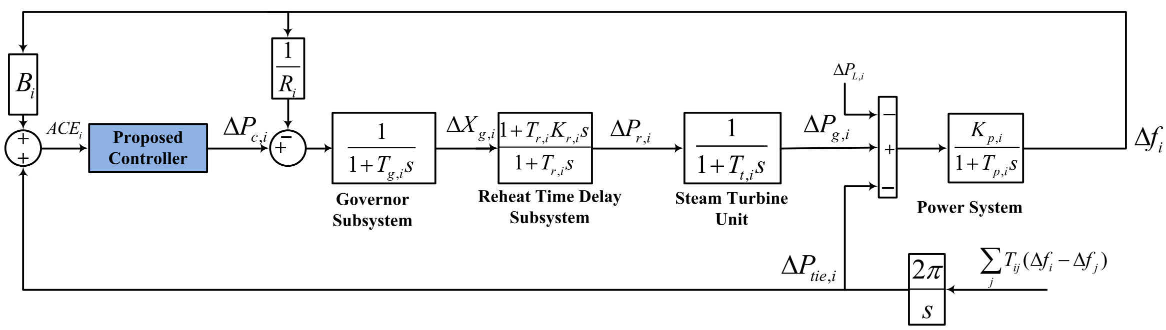

FIGURE 2. Structure of a reheat thermal power system with a control area.

Thus, it is important to make the fundamental presumption that the given variable in (15) is adequately similar to a sinusoidal oscillation and can be defined as follows:

$$y = A'.sin(\omega_0 t) \tag{16}$$

where ω_0 denotes the oscillation frequency and A' represents the amplitude.

The aforementioned assumption is reasonable since nonlinearities can display periodic oscillations that are approximately sinusoidal. According to analysis in [38], the backlash nonlinearity typically results in a continuous sinusoidal signal with a natural duration of 2 seconds with $\omega_0 = 2\pi f_0$, where $f_0 = 0.5$. As the given function $G(z, \dot{z})$ in Eq. (15) is a complicated and periodical function, it can be expressed in a Fourier series form as in the following equation [38]:

$$G(z, \dot{z}) = G^0 + M_1 z + \frac{M_2}{\omega_0}\dot{z} + \dots \tag{17}$$

As in [6], we consider the first three terms to resolve (17). As the backlash nonlinearity is symmetrically established in origin, thus $G^0 = 0$, and the Fourier co-officiants are given as $M_1 = 0.8$ and $M_1 = -0.2$ according to [6]. Hence, (17) can be reformulated as follows:

$$G(z, \dot{z}) = 0.8z - \frac{0.2}{\pi}\dot{z} + \dots \tag{18}$$

Therefore, the following equation explains the transfer function of the considered governor dead band (GDB):

$$G_{g,i}(s) = \frac{0.8 - \frac{0.2}{\pi}s}{1 + T_{g,i}s} \tag{19}$$

3) GENERATION RATE CONSTRAINT (GRC)

The rate at which the output power $\Delta\dot{P}_g$ of steam turbine systems can be adjusted is subject to limitations imposed by thermodynamic and mechanical constraints in real applications. This constraint is commonly referred to as the Gas Turbine Rate Constraint (GRC) [6]. Rate constraints are considered in the system to mitigate significant fluctuations in process variables, such as pressure and temperature, with the primary objective of ensuring the safety and integrity of

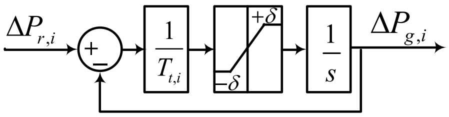

FIGURE 3. **Model of GRC dynamics.**

the system equipment [39]. In this paper, the GRC of 10% per minute is considered in reheat thermal power systems in all areas [22], i.e.

$$\Delta \dot{P}_g = 0.0017(\text{p.u MW/s}) \tag{20}$$

Therefore, the GRC, which is represented by a limiter bounded by ($\delta = \pm 0.0017$), is added to the turbine units in the power system for each zone to constrain the generation ramp rate for the reheat thermal and electrical power plants, as described in Fig. 3 [14], [22], [39].

4) BOILER DYNAMICS

The fluctuation in generating units is launched by the boiler dynamic control action and turbine control valves. A boiler dynamic can be defined as an instrument responsible for generating steam under pressure, and the structure of boiler dynamics is shown in Fig. 4, where C_B, T_F, T_D, T_{RB}, T_{IB}, and K_{IB} are the boiler storage time constant (s), the fuel system time constant (s), the fuel firing system delay time (s), the lead-lag compensator time (s), the proportional-integral ratio of gains, and the boiler integrator gain, respectively. It is seen from Fig. 4 that the boiler system is composed of the fuel and steam flow dynamics, the boiler drum pressure, and the combustion controls. The readers can refer to Ref. [40] for details of the boiler dynamics model.

5) WIND TURBINE MODEL-BASED LFC

A wind turbine (WT) is a unit for transferring kinetic energy obtained from wind into electrical energy. The WT model for frequency control is displayed in Fig. 5 [36], [37]. To estimate the random wind output power variations in this model, the wind speed is multiplied by the random speed fluctuation, which is derived from the white noise block in MATLAB/Simulink. The following equation describes the output power of the WT model:

$$P_{WT} = 0.5\rho A_T c_p(\lambda, \beta) V_{WT}^3 \tag{21}$$

where V_{WT} is rated wind speed in m/s, A_T is swept area by rotor in m^2, and ρ is air density in kg/m^3. c_p represents the rotor blade coefficient, which can be described by the following equation:

$$c_p(\lambda, \beta) = c_1\left(\frac{c_2}{\lambda_I} - c_3\beta - c_4\beta^3 - c_5\right)e^{\frac{-c_6}{\lambda_I}} + c_7\lambda_T \tag{22}$$

where $c_1 - c_7$ are wind turbine coefficients, β is the pitch angle, and λ_T corresponds to the optimum tip-speed ratio (TSR), which can be defined as follows:

$$\lambda_T = \lambda_T^{opt} = \frac{\omega_T \times r_T}{V_{WT}} \tag{23}$$

where r_T is the rotor radius and λ_I represents the intermittent TSR, which can be calculated as follows:

$$\frac{1}{\lambda_I} = \frac{1}{\lambda_T + 0.08\beta} - \frac{0.035}{\beta^3 + 1} \tag{24}$$

Furthermore, the wind turbine dynamic model can be interpreted as follows:

$$\Delta \dot{P}_{WT,i} = \frac{1}{T_{WT,i}} P_{WT,i} - \frac{1}{T_{WT,i}} \Delta P_{WT,i} \tag{25}$$

Therefore, the aforementioned equations in terms of dynamic models of reheat thermal and wind turbines can be represented in the state space model as (26), shown at the bottom of the next page.

The detailed model of a four-area interconnected hybrid power system considering the boiler dynamic, the GDB, and GRC constraints is depicted in Fig. 6; thus, this model is utilized to validate the proposed method.

III. CONTROLLER DESIGN

This section introduces the design of $\alpha(t)$-MF-ABFFONSMC, whose architecture is displayed in Fig. 7. The designed $\alpha(t)$-MF-ABFFONSMC strategy is comprised of ULM-based SMDO, PD controller, and adaptive barrier-function fractional-order nonlinear sliding mode control (ABF-FONSMC). The SMDO is employed to observe and compensate for the uncertain system dynamics. The PD controller is designed to stabilize the closed-loop system. Correspondingly, the SMDO-iPD controller is implemented. Whereas, the estimation error of SMDO will affect the control performance; therefore, ABFFONSMC is constructed to eliminate the impact of estimation errors and improve the control performance. Furthermore, the adaptive parameter based on the barrier function is established to approximate the unknown upper boundary of the estimation error so as to avoid undesired chattering. Correspondingly, the $\alpha(t)$-MF-ABFFONSMC can be realized. Finally, the MPA is introduced to optimize the parameters of the proposed controller by employing the integral time weighted-absolute error (ITAE) criterion.

A. SMDO-IPD CONTROLLER DESIGN

Consider the following ultra-local model algorithm for a general unknown non-linear dynamic model with single-input, single-output (SISO) as [8], [29]:

$$y^{(m)}(t) = \varepsilon(t) + \alpha u(t) \tag{27}$$

where $y(t)$ represents the system output variable, m is the order derivative of the output signal, which can be selected as 1 or 2, $u(t)$ is the control input variable, and α is the input gain. $\varepsilon(t)$ denotes an unknown term that can be estimated using the input signal $u_i(t)$ and output signal $y(t)$. $\varepsilon(t)$ not only involves the influence of unknown dynamics of the plant but also includes any external disturbances.

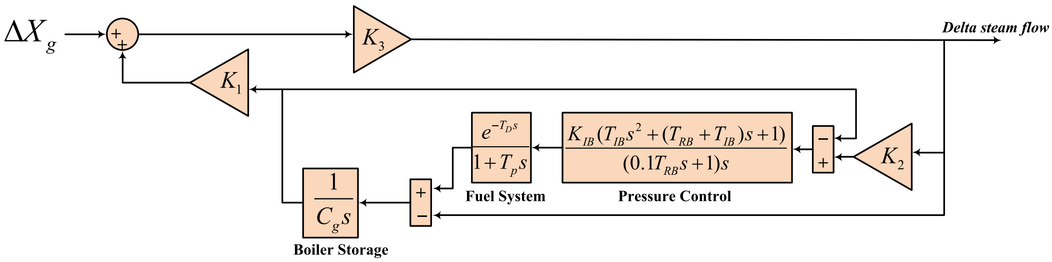

FIGURE 4. Model of boiler dynamics.

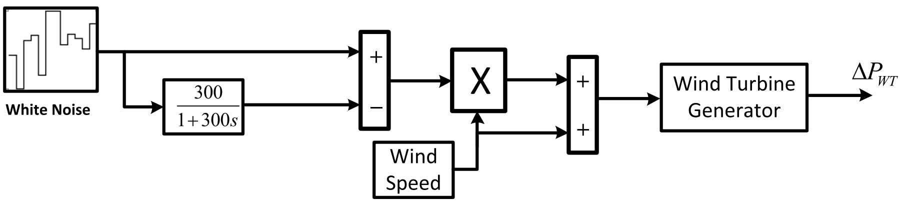

FIGURE 5. Simplified model of the wind power generating source.

The SMDO-iPD controller can be designed as follows [8], [29]

$$u_{\text{SMDO-iPD}}(t) = \frac{1}{\alpha}\left[-\hat{\varepsilon}(t) + \ddot{y}_{\mathrm{d}}^{*}(t) + K_{\mathrm{p}}e(t) + K_{\mathrm{d}}\frac{\mathrm{d}e(t)}{\mathrm{d}t}\right] \tag{28}$$

where $y_{\mathrm{d}}(t)$ is the output reference trajectory, K_{p} and K_{d} are the proportional and derivative gains of the PD controller, $e(t)$ denotes the tracking error signal, which is the difference between the reference trajectory $y(t)$ and the current value of the plant output. $y_{\mathrm{d}}(t)$, $\hat{\varepsilon}(t)$ denotes the estimated value of $\varepsilon(t)$. Hence, the steady error of the system can be acquired by adjusting the parameters K_{p} and K_{d}.

In this paper, a sliding mode disturbance observer (SMDO) is used to estimate the lumped uncertainties $\varepsilon(t)$ via the control input and output data. From the view of (27), denote $\xi_1 \triangleq y(t)$ and $\xi_2 \triangleq \dot{y}(t)$. Then, (27) can be rewritten as follows:

$$\begin{aligned} \dot{\xi}_1 &= \xi_2 \\ \dot{\xi}_2 &= \alpha u(t) + \varepsilon(t) \end{aligned} \tag{29}$$

Thus, to observe the unknown system dynamics, the SMDO can be formulated as follows:

$$\begin{aligned} \dot{\hat{\xi}}_1 &= \hat{\xi}_2 + \alpha u(t) + \mu_1|\xi_1 - \hat{\xi}_1|^{1/2}sgn(\xi_1 - \hat{\xi}_1) \\ \dot{\hat{\xi}}_2 &= \mu_2 sgn(\xi_1 - \hat{\xi}_1) \end{aligned} \tag{30}$$

where $\hat{\xi}_1$ and $\hat{\xi}_2$ represent the state variables of SMDO, and μ_1 and μ_2 are updated positive parameters. Thus, the estimated value of uncertain system dynamics $\varepsilon(t)$ can be calculated, where $\hat{\varepsilon}(t) = \hat{\xi}_2$. From (29) and (30), the

$$\begin{aligned}
\begin{pmatrix} \Delta\dot{f}_i \\ \Delta\dot{P}_{WT,i} \\ \Delta\dot{P}_{tie,i} \\ \Delta\dot{P}_{g,i} \\ \Delta\dot{X}_{g,i} \\ \Delta\dot{P}_{r,i} \end{pmatrix} &= \begin{pmatrix} -\frac{1}{T_{p,i}} & -\frac{1}{H_{WT,i}} & -\frac{K_{p,i}}{T_{p,i}} & \frac{K_{p,i}}{T_{p,i}} & 0 & 0 \\ -\frac{1}{T_{WT,i}} & 0 & 0 & 0 & 0 & 0 \\ 2\pi\sum_i T_{i,j} & 0 & 0 & 0 & 0 & 0 \\ 0 & 0 & 0 & -\frac{1}{T_{t,i}} & 0 & \frac{1}{T_{t,i}} \\ -\frac{1}{T_{g,i}R_i} & 0 & 0 & 0 & -\frac{1}{T_{g,i}} & 0 \\ -\frac{K_{r,i}}{T_{g,i}R_i} & 0 & 0 & 0 & \frac{1}{T_{r,i}} - \frac{K_{r,i}}{T_{g,i}} & \frac{1}{T_{r,i}} \end{pmatrix} \begin{pmatrix} \Delta f_i \\ \Delta P_{WT,i} \\ \Delta P_{tie,i} \\ \Delta P_{g,i} \\ \Delta X_{g,i} \\ \Delta P_{r,i} \end{pmatrix} \\
&+ \begin{pmatrix} -\frac{K_{p,i}}{T_{g,i}} & 0 \\ 0 & \frac{1}{T_{WT,i}} \\ 0 & 0 \\ 0 & 0 \\ 0 & 0 \\ 0 & 0 \end{pmatrix} \begin{pmatrix} \Delta P_{L,i} \\ P_{WT,i} \end{pmatrix} + \begin{pmatrix} 0 \\ 0 \\ 0 \\ 0 \\ \frac{1}{T_{g,i}} \\ 0 \end{pmatrix} \Delta P_{c,i}
\end{aligned} \tag{26}$$

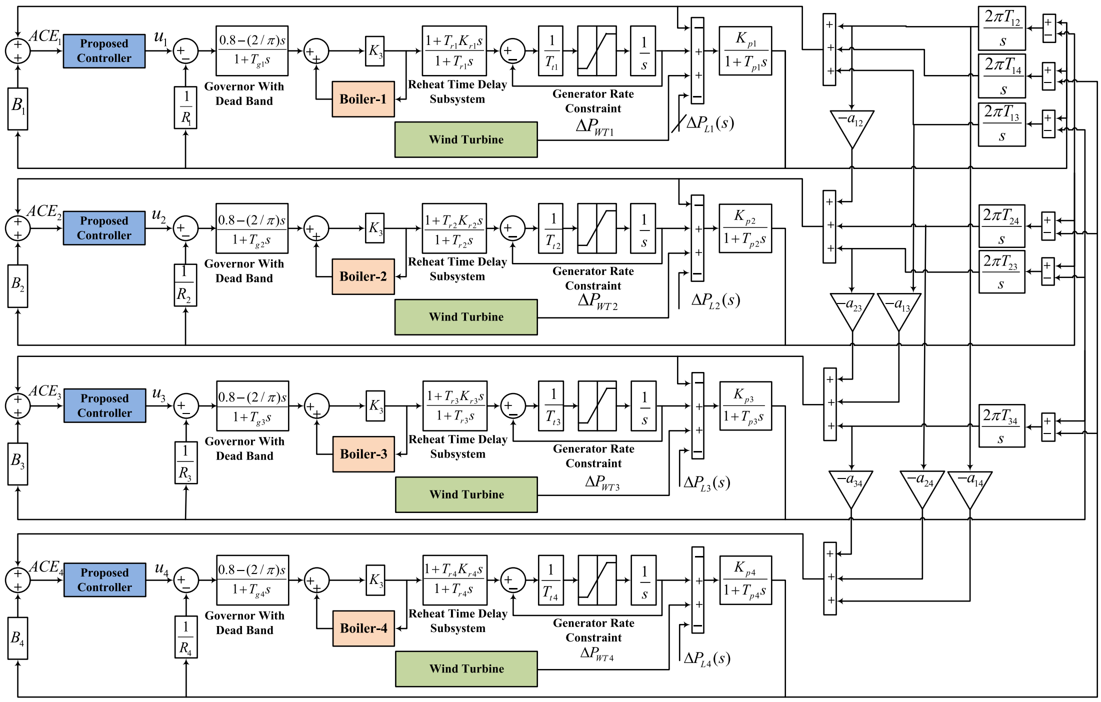

FIGURE 6. Structure of the four-area interconnected hybrid power system model.

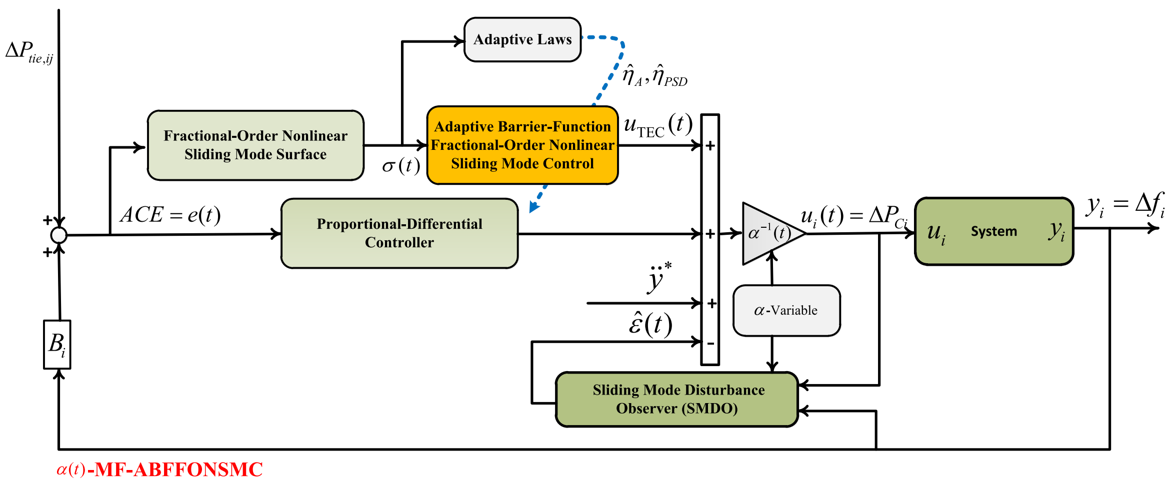

FIGURE 7. Structure of the proposed $\alpha(t)$-MF-ABFFONSMC method.

estimation error dynamic is given as

$$\begin{aligned}\dot{\tilde{\xi}}_1 &= \tilde{\xi}_2 - \mu_1|\tilde{\xi}_1|^{1/2}sgn(\tilde{\xi}_1)\\ \dot{\tilde{\xi}}_2 &= \varrho(t) - \mu_2 sgn(\tilde{\xi}_1)\end{aligned} \tag{31}$$

where $\tilde{\xi}_1 = \xi_1 - \hat{\xi}_1$ and $\tilde{\xi}_2 = \xi_2 - \hat{\xi}_2$. $\varrho(t) = \dot{\varepsilon}(t)$ with $|\varrho(t)| < K$, K is a positive constant. According to Refs. [41], [42], and [43], the finite time convergence of the estimation error (31) is ensured by defining the parameters of SMDO as:

$$\begin{aligned}\mu_1 &= 1.5\sqrt{K}\\ \mu_2 &= 1.1K\end{aligned} \tag{32}$$

Theorem 1: Consider the four-area interconnected hybrid power system (26) re-constructed by the ultra-local model (27) with the designed SMDO-iPD control law (28), using the reasonable coefficients of K_p and K_d, and α, the stability of a closed-loop system is ensured, and control error asymptotically will be converged within a bound, i.e.,

$$|e(t)| \leq \frac{\sqrt{\Pi(0)}}{\sqrt{\mu_1}}\exp\left(-\frac{\mu_3}{2\mu_2}t\right) + \frac{2\mu_2^2\eta}{\mu_1\mu_3} \tag{33}$$

Proof: Substituting (28) into (27), the error equation can be defined as

$$\ddot{e}(t) = -K_\text{p}e(t) - K_\text{d}\dot{e}(t) + \tilde{\varepsilon}(t) \tag{34}$$

TABLE 1. System parameters.

Parameter	Value	Parameter	Value
Reheat thermal parameters [14], [15], [21]			
$T_{t,i}$	0.3 (s)	T_{ij}	0.0707 (p.u.MW)
R_i	2.4 (Hz/p.u.MW)	Boiler (gas or oil fired) data	
B_i	0.425 (p.u.MW/Hz)	K_1	0.85
$T_{g,i}$	0.08 (s)	K_2	0.095
$T_{r,i}$	10 (s)	K_3	0.92
$K_{r,i}$	0.5	T_F	10 (s)
T_{ij}	0.08674	T_{IB}	26
T_{pi}	20 (s)	T_{RB}	69 (s)
K_{pi}	120 (Hz/p.u.MW)	C_B	200 (s)
a_{ij}	-1.0 (p.u)	T_D	0 (s)
		K_{IB}	0.03
Wind turbine system parameters [36], [37]:			
P_{WT}	3000kW	c_1	0.3915
V_{WT}	12 m/s	c_2	116
ρ	1.225 kg.m^3	c_3	0.4
A_T	5905 m^2	c_4	0
r_t	43.63 m	c_5	5
n_T	22.5 rpm	c_6	21
		c_7	0.0192

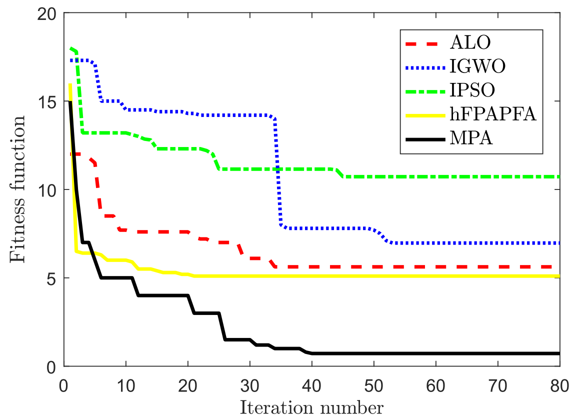

FIGURE 8. The fitness function convergence of the applied optimization algorithms.

where $\tilde{\varepsilon}(t) = \varepsilon(t) - \hat{\varepsilon}(t)$ denotes the estimation error.

Due to the SMDO characteristics, the estimation error $\tilde{\varepsilon}(t)$ is bounded as $\tilde{\varepsilon}(t) \leq \eta$, with $\eta > 0$. Then, define new state variables as $z_1(t) \triangleq e(t)$ and $z_2(t) \triangleq \dot{e}(t)$; therefore, (34) can be rewritten in a state-space form as:

$$\dot{z}(t) = Az(t) + B\tilde{\varepsilon}(t) \tag{35}$$

with
$A = \begin{bmatrix} 0 & 1 \\ -K_p & -K_d \end{bmatrix}, \quad B = \begin{bmatrix} 0 \\ 1 \end{bmatrix}$

Then, the Lyapunov function is selected as follows:

$$\Pi(t) = z^{\mathrm{T}}(t)\Xi z(t) \tag{36}$$

where Ξ denotes a symmetric positive definite matrix. Then, differentiating (36) yields:

$$\begin{aligned}\dot{\Pi}(t) &= \dot{z}^{\mathrm{T}}(t)\Xi z(t) + z^{\mathrm{T}}(t)\Xi\dot{z}(t) \\ &= \dot{z}^{\mathrm{T}}(t)\left\{A^{\mathrm{T}}\Xi + \Xi A\right\} z(t) + 2z^{\mathrm{T}}(t)\Xi B\tilde{\varepsilon}(t)\end{aligned} \tag{37}$$

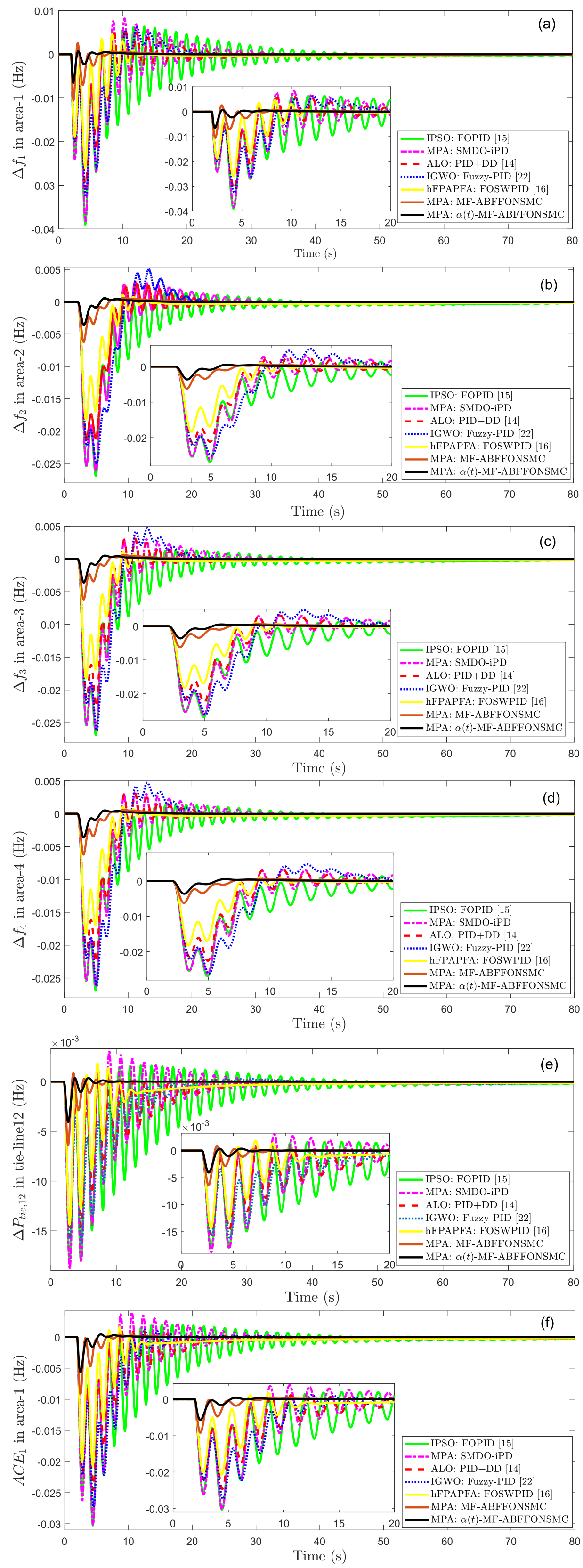

FIGURE 9. The dynamic performance for the first scenario:(a),(b),(c) and (d) show frequency deviations in a four area,(e) represents the power deviation in tie-line−12 $\Delta P_{tie,12}$, and (f) displays the ACE deviation in area−1.

TABLE 2. Optimal parameters of all applied controllers.

Area	Controller	Parameters								
Area-1	IPSO: FOPID [15]	K_p	K_i	K_d	γ	ς				
		0.095	0.510	0.325	0.84	0.9				
	MPA: SMDO-iPD	K_p	K_d			α				
		0.105	0.230			9.2				
	ALO: PID+DD [14]	K_p	K_i	K_d	K_{dd}					
		0.217	0.29	0.1174	0.0085					
	IGWO:Fuzzy-PID [22]	K_p	K_i	K_d	K_1	K_2				
		0.113	1.31	0.512	-0.86	-1.06				
	hFPAPFA: FOSWPID [16]	K_p	K_i	K_d	λ_1	b_1	c_1			
		1.65	0.82	1.2	0.91	0.95	0.44	0.96		
	MPA: $\alpha(t)$-MF-ABFFONSMC	Ω	q_1	q_2	b_1	b_2	a_1	a_2	ν	λ
		10.11	0.650	0.250	3.54	2.42	0.93	0.54	0.5	1.34
Area-2	IPSO: FOPID [15]	K_p	K_i	K_d	γ	ς				
		0.115	0.49	0.425	0.9	0.85				
	MPA: SMDO-iPD	K_p	K_d			α				
		0.13	0.19			8.9				
	ALO: PID+DD [14]	K_p	K_i	K_d	K_{dd}					
		0.24	0.31	0.21	0.021					
	IGWO:Fuzzy-PID [22]	K_p	K_i	K_d	K_1	K_2				
		0.13	1.4	0.44	-0.78	-1.1				
	hFPAPFA: FOSWPID [16]	K_p	K_i	K_d	λ_1	b_1	c_1			
		2.1	0.79	1.5	0.82	0.94	0.44	0.99		
	MPA: $\alpha(t)$-MF-ABFFONSMC	Ω	q_1	q_2	b_1	b_2	a_1	a_2	ν	λ
		10.11	0.70	0.240	3.43	2.2	0.883	0.65	0.55	1.29
Area-3	IPSO: FOPID [15]	K_p	K_i	K_d	γ	ς				
		0.124	0.39	0.51	0.89	0.92				
	MPA: SMDO-iPD	K_p	K_d			α				
		0.21	0.098			9.7				
	ALO: PID+DD [14]	K_p	K_i	K_d	K_{dd}					
		0.33	0.27	0.19	0.036					
	IGWO:Fuzzy-PID [22]	K_p	K_i	K_d	K_1	K_2				
		0.15	1.2	0.39	-0.68	-1.21				
	hFPAPFA: FOSWPID [16]	K_p	K_i	K_d	λ_1	b_1	c_1			
		1.99	0.85	1.7	0.71	0.87	0.44	0.96		
	MPA: $\alpha(t)$-MF-ABFFONSMC	Ω	q_1	q_2	b_1	b_2	a_1	a_2	ν	λ
		11.5	0.81	0.39	2.31	1.98	0.79	0.77	0.63	1.18
Area-4	IPSO: FOPID [15]	K_p	K_i	K_d	γ	ς				
		0.13	0.34	0.6	0.91	0.88				
	MPA: SMDO-iPD	K_p	K_d			α				
		0.19	0.11			8.9				
	ALO: PID+DD [14]	K_p	K_i	K_d	K_{dd}					
		0.38	0.3	0.2	0.029					
	IGWO:Fuzzy-PID [22]	K_p	K_i	K_d	K_1	K_2				
		0.17	1.3	0.4	-0.7	-1.13				
	hFPAPFA: FOSWPID [16]	K_p	K_i	K_d	λ_1	b_1	c_1			
		2.1	0.87	1.8	0.69	0.8	0.5	0.97		
	MPA: $\alpha(t)$-MF-ABFFONSMC	Ω	q_1	q_2	b_1	b_2	a_1	a_2	ν	λ
		12	0.84	0.4	2.4	2	0.8	0.73	0.59	1.21

TABLE 3. Dynamic performance for the first scenario regarding the settling time and peak undershoot.

Controller	Settling time (s) for 5%band						Peak undershoot (-ve)(pu.Hz)					
	Δf_1	Δf_2	Δf_3	Δf_4	ΔP_{tie1}	ACE_1	Δf_1	Δf_2	Δf_3	Δf_4	$\Delta P_{tie,12}$	ACE_1
IPSO: FOPID [15]	31.51	23.29	23.32	23.32	34.47	30.99	0.0390	0.0269	0.0269	0.0269	0.0181	0.0303
MPA: SMDO-iPD	22.90	21.89	21.87	21.87	24.12	21.37	0.0383	0.0262	0.0263	0.0263	0.0188	0.0302
ALO: PID+DD [14]	19.53	18.61	16.74	16.74	22.82	20.83	0.0310	0.0215	0.0226	0.0226	0.0156	0.0246
IGWO: Fuzzy-PID [22]	18.40	17.62	17.63	17.63	19.86	16.74	0.0326	0.0251	0.0262	0.0262	0.0162	0.0273
hFPAPFA: FOSWPID [16]	13.94	14.15	14.15	13.17	16.52	12.62	0.0260	0.0183	0.0183	0.0183	0.0144	0.0207
MPA: MF-ABFFONSMC	10.67	13.16	13.16	13.17	6.43	6.30	0.0106	0.0062	0.0062	0.0062	0.0064	0.0092
MPA: $\alpha(t)$-MF-ABFFONSMC	8.18	11.17	11.20	11.20	6.11	6.0248	0.0065	0.0036	0.0036	0.0036	0.0041	0.0056

By selecting the suitable coefficients of K_p and K_d such that A is a Hurwitz matrix, a positive definite matrix Q exists, satisfying $-Q = A^{\mathrm{T}}\Xi + \Xi A$.

Therefore, one can get the following inequality:

$$\dot{\Pi}(t) = -\dot{z}^{\mathrm{T}}(t)Qz(t) + 2z^{\mathrm{T}}(t)\Xi B\tilde{\varepsilon}(t)$$

TABLE 4. Dynamic performance for the first scenario regarding the IAE and TAE.

Controller	IAE						ITAE					
	Δf_1	Δf_2	Δf_3	Δf_4	ΔP_{tie1}	ACE_1	Δf_1	Δf_2	Δf_3	Δf_4	$\Delta P_{tie,12}$	ACE_1
IPSO: FOPID [15]	0.2060	0.1489	0.1491	0.1491	0.1255	0.1865	2.956	1.930	1.942	1.942	1.957	2.711
MPA: SMDO-iPD	0.1535	0.1208	0.1212	0.1212	0.0933	0.1417	1.651	1.223	1.227	1.227	1.206	1.660
ALO: PID+DD [14]	0.1195	0.0998	0.1001	0.1001	0.0806	0.1182	1.310	1.092	1.081	1.081	1.058	1.426
IGWO: Fuzzy-PID [22]	0.1456	0.1392	0.1386	0.1386	0.0942	0.1358	1.496	1.421	1.451	1.451	1.150	1.456
hFPAPFA: FOSWPID [16]	0.0848	0.0756	0.0756	0.0756	0.0619	0.0928	1.078	1.031	1.031	1.031	0.9696	1.385
MPA: MF-ABFFONSMC	0.0182	0.0189	0.0164	0.0164	0.0091	0.0150	0.160	0.158	0.158	0.158	0.087	0.145
MPA: $\alpha(t)$-MF-ABFFONSMC	0.0084	0.0078	0.0078	0.0078	0.0052	0.0080	0.063	0.064	0.064	0.064	0.044	0.068

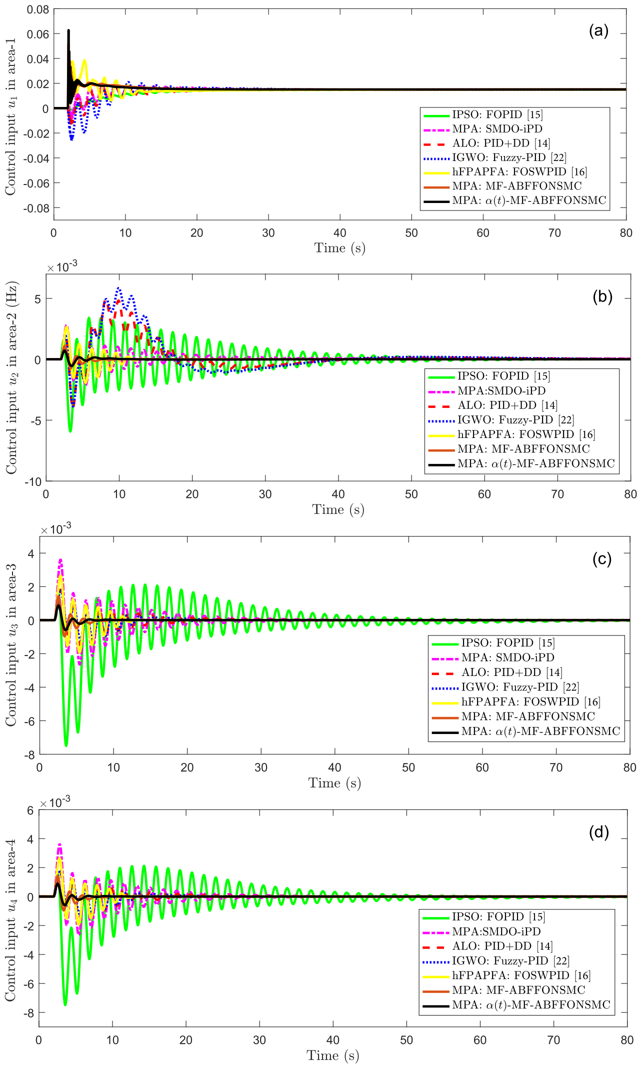

FIGURE 10. Control inputs of all areas: (a) u_1 in area-1, (b) u_2 in area-2, (c) u_3 in area-3, and (d) u_4 in area-4.

$$\leq -\mu_3 \parallel z(t) \parallel^2 + 2 \parallel z(t) \parallel \Xi|\tilde{\varepsilon}(t)|$$
$$\leq -\frac{\mu_3}{\mu_2}\Pi(t) + \frac{2\sqrt{\Pi(t)}}{\mu_1}\mu_2\eta \tag{38}$$

where $\mu_1 \parallel z(t) \parallel^2 \leq z^{\mathrm{T}}(t)\Xi z(t) \leq \mu_2 \parallel z(t) \parallel^2$, $\mu_3 \parallel z(t) \parallel^2 \leq z^{\mathrm{T}}(t)Qz(t) \leq \mu_4 \parallel z(t) \parallel^2$. Further, one obtains

$$\frac{d}{dt}\sqrt{\Pi(t)} = -\frac{1}{2\sqrt{\Pi(t)}}\dot{\Pi}(t) \leq -\frac{\mu_3}{2\mu_2}\sqrt{\Pi(t)} + \frac{\mu_2\eta}{\sqrt{\mu_2}} \tag{39}$$

Since $\mu_1 \parallel z(t) \parallel^2 \leq \Pi(t)$, we have

$$|e(t)| \leq \parallel z(t) \parallel \leq \frac{\sqrt{\Pi(t)}}{\sqrt{\mu_1}} \leq \frac{\sqrt{\Pi(0)}}{\sqrt{\mu_1}}\exp\left(-\frac{\mu_3}{2\mu_2}t\right) + \frac{2\mu_2^2\eta}{\mu_1\mu_3}\int_0^t \exp\left(-\frac{\mu_3}{2\mu_2}(t-\tau)\right)d\tau$$
$$\leq \frac{\sqrt{\Pi(0)}}{\sqrt{\mu_1}}\exp\left(-\frac{\mu_3}{2\mu_2}t\right) + \frac{2\mu_2^2\eta}{\mu_1\mu_3} \tag{40}$$

Hence, the stability of the closed-loop system is ensured, and the control error asymptotically will be converged and bounded with (40). This completes the proof.

B. ADAPTIVE BARRIER-FUNCTION FRACTIONAL-ORDER NONLINEAR SLIDING MODE CONTROL

From the above subsection, the designed SMDO-iPD controller can only achieve asymptotic and bounded convergence. To remove and compensate for the impact of SMDO estimation errors on trajectory tracking precision and avoid input chattering, ABFFONSMC is constructed and inserted into the SMDO-IPD structure. According to the ULM principle, (27) can be rewritten as follows

$$\ddot{y}(t) = \varepsilon(t) + \alpha(t)u(t) \tag{41}$$

where $\alpha(t)$ is the updated parameter and its description will be given in (59) later.

Based on the designed SMDO-iPD structure (30) and updated parameter $\alpha(t)$, the control law of $\alpha(t)$-MF-ABFFONSMC can be formulated as follows:

$$u(t) = \frac{\ddot{y}(t) - \hat{\varepsilon}(t) + K_{\mathrm{p}}e(t) + K_{\mathrm{d}}\dot{e}(t)}{\alpha(t)} + \frac{u_{TEC}(t)}{\alpha(t)} \tag{42}$$

where $u_{TEC}(t)$ represents the ABFFONSMC sub-controller law for tracking error convergence (TEC) to be designed. Substituting (42) into (27), a new error equation can be obtained as follows:

$$\ddot{e}(t) + K_{\mathrm{p}}e(t) + K_{\mathrm{d}}\dot{e}(t) - \tilde{\varepsilon}(t) + u_{TEC}(t) = 0 \tag{43}$$

Then, defining $x_1(t) \triangleq e(t)$ and $x_2(t) \triangleq \dot{e}(t)$, one further has:

$$\dot{x}_1(t) = x_2(t)$$
$$\dot{x}_2(t) = -K_{\mathrm{p}}x_1(t) - K_{\mathrm{d}}x_2(t) + \tilde{\varepsilon}(t) - u_{TEC}(t) \tag{44}$$

In the SMC design approach, the selection of sliding surfaces significantly influences system performance and stability. The sliding surface is constructed in such a way that when it reaches the origin, the system can achieve

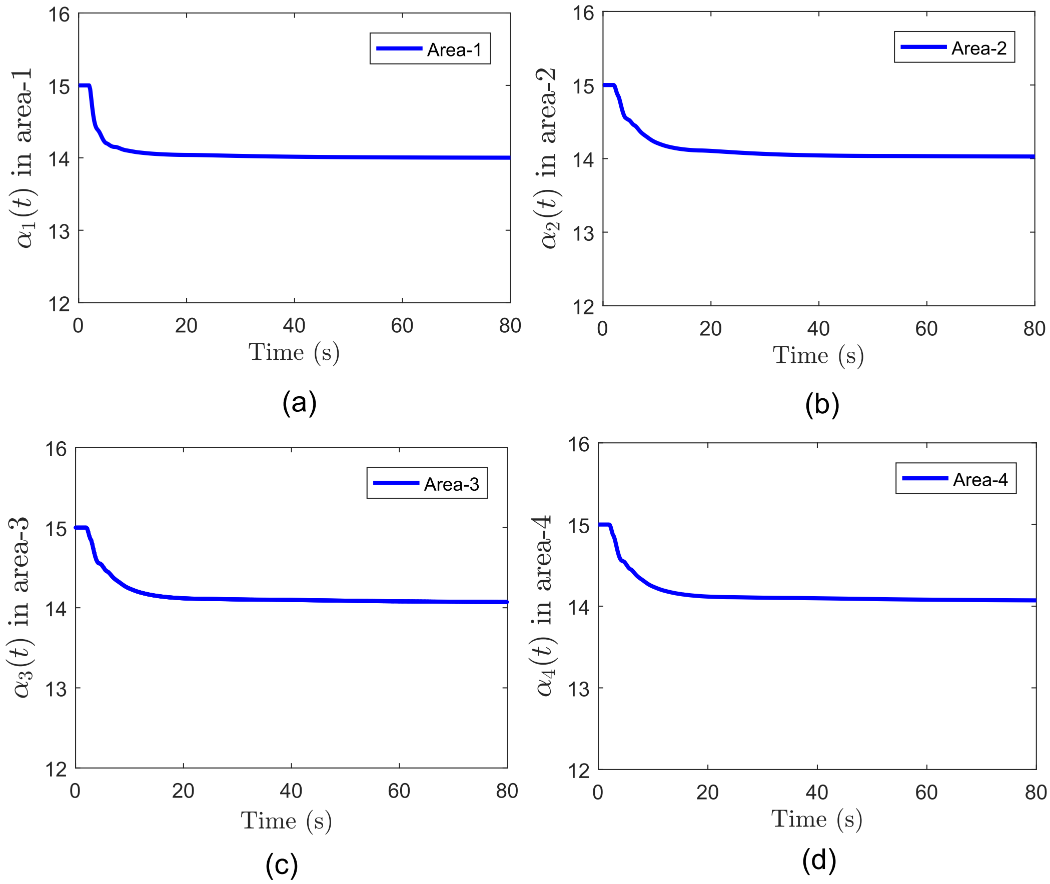

FIGURE 11. Updating curve of $\alpha(t)$ of controlled system with $\alpha(t)$-MF-ABFFONSMC: (a) Area-1, (b) Area-2, (c) Area-3, and (d) Area-4.

the expected performance. Thus, to realize an SMC with a nonlinear sliding manifold for the dynamic system (27), the fractional-order nonsingular terminal sliding mode (FONTSM) surface is proposed as:

$$\sigma(t)=x_2(t)+b_1\mathcal{D}^{q_1}[sgn(x_1(t))^{a_1}]+b_2\mathcal{D}^{q_2-1}[sgn(x_1(t))^{a_2}] \tag{45}$$

where $a_1, a_2, b_1, b_2, q_1, q_2$ are positive constants.

Remark 1: It can be observed that the proposed fractional order sliding mode (FOSM) surface in [32] and [45] is given as

$$\sigma(t)=\dot{e}(t)+b_2\mathcal{D}^{q_2-1}[sgn(e(t))^{a_2}] \tag{46}$$

When the trajectory of the controlled system reaches the FOSM surface which is defined in (46) at $\sigma(t) = 0$, the following equality holds

$$\dot{e}(t)=-b_2\mathcal{D}^{q_2-1}[sgn(e(t))^{a_2}]=-b_2\mathcal{I}^{1-q_2}[sgn(e(t))^{a_2}] \tag{47}$$

where $0 < q_2 < 1$. Hence, it is noticed that the right-hand term represents a FO integral term. This type of design may lead to degradation in the overall control performance. Conversely, our designed FONTSM surface (45) considers this issue by incorporating an additional fractional order (FO) differential term, denoted as $b_1\mathcal{D}^{q_1}[sgn(x_1(t))^{a_1}]$, thereby ensuring robustness and improved performance.

Next, to achieve a robust SMC, the global sliding manifold is defined as follows:

$$\vartheta(t)=\kappa(\sigma(t)-\sigma(0)exp(-\nu t)) \tag{48}$$

where κ is designed parameter, and ν is the positive constant.

Remark 2: In contrast to the sliding manifold, the nonlinear global sliding surface forces the tracking error to attain the manifold from the initial instance. Consequently, the robust behavior of the system in the presence of perturbation is ensured.

Then, by taking the first time derivative for (48), one has:

$$\begin{aligned}\dot{\vartheta}(t)&=\kappa[\dot{\sigma}(t)+\nu\sigma(0)exp(-\nu t)]\\&=\kappa[q_1b_1\mathcal{D}^{q_1+1}[sgn(x_1(t))^{a_1}]+q_2b_2\mathcal{D}^{q_2}[sgn(x_1(t))^{a_2}]\\&\quad\times\dot{x}_2(t)+\nu\sigma(0)exp(-\nu t)]\end{aligned} \tag{49}$$

By substituting $\dot{x}_2(t)$ from (44) into (49), it yields:

$$\begin{aligned}&\dot{\vartheta}(t)\\&=\kappa\Big[-K_{\mathrm{p}}x_1(t)-K_{\mathrm{d}}x_2(t)+\tilde{\varepsilon}(t)+q_1b_1\mathcal{D}^{q_1+1}[sgn(x_1(t))^{a_1}]\\&\quad+q_2b_2\mathcal{D}^{q_2}[sgn(x_1(t))^{a_2}]+\nu\sigma(0)exp(-\nu t)-u_{TEC}(t)\Big]\end{aligned} \tag{50}$$

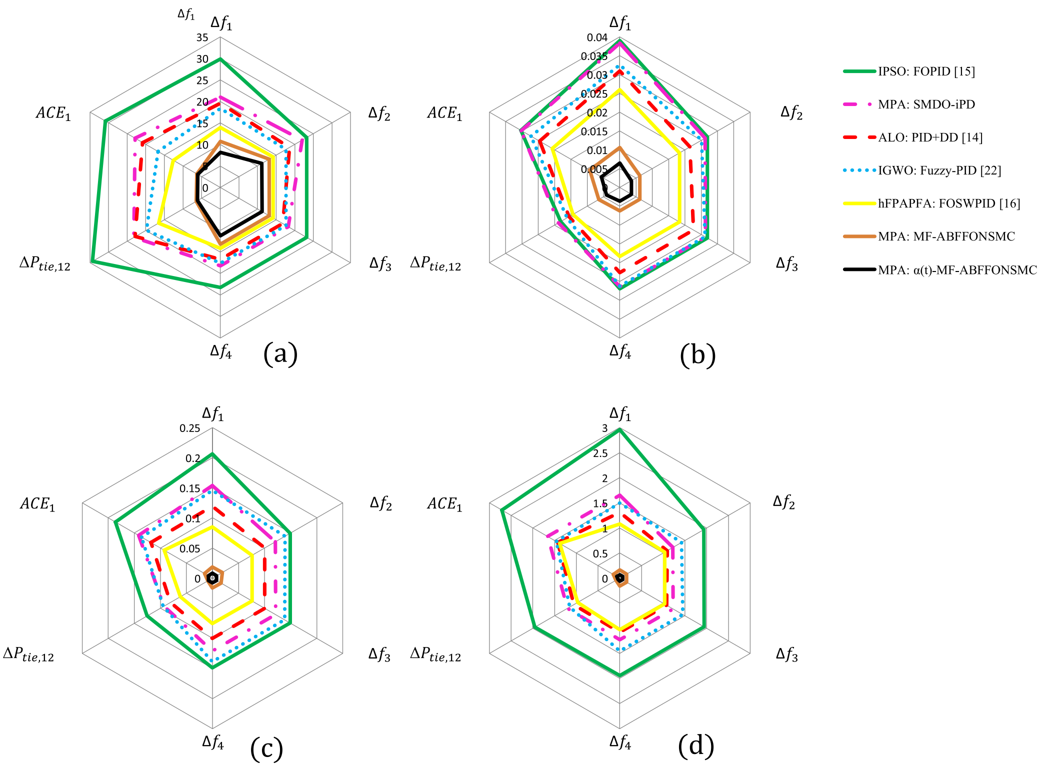

FIGURE 12. The graphical representation of performance indexes for the first scenario: (a) Shows the settling time (s) for 5%band (b) Peak undershoot (-ve)(pu. Hz), (c) IAE and (d) ITAE.

In order to ensure $\vartheta(t)$ is convergent and stable, the compensated control law $u_{TEC}(t)$ is constructed with two terms as follows:

$$u_{TEC}(t) = u^{eq}_{TEC}(t) + u^{re}_{TEC}(t) \tag{51}$$

where $u^{eq}_{TEC}(t)$ and $u^{re}_{TEC}(t)$ represent the equivalent control law and the reaching control law, respectively.

The necessary condition is $\dot{\vartheta}(t) = 0$ to stay on the sliding surface $\vartheta(t)$, while to attain an equivalent control law from (50), the estimation error caused by SMDO $\tilde{\varepsilon}(t)$ is not considered. Thus, the equivalent control law $u^{eq}_{TEC}(t)$ is given as follows:

$$\begin{aligned} &u^{eq}_{TEC}(t) \\ &= \Big[-K_p x_1(t) - K_d x_2(t) + q_1 b_1 \mathcal{D}^{q_1+1}[sgn(x_1(t))^{a_1}] \\ &\quad + q_2 b_2 \mathcal{D}^{q_2}[sgn(x_1(t))^{a_2}] + \nu\sigma(0)exp(-\nu t)\Big] \end{aligned} \tag{52}$$

To guarantee that the sliding manifold can reach its origin $\vartheta(t) = 0$, it is necessary to design a reasonable auxiliary control law $u^{re}_{TEC}(t)$. However, the estimation error caused by SMDO $\tilde{\varepsilon}(t)$ is considered an unknown term, and there is no exact information about its upper and lower boundaries; hence, the term $\tilde{\varepsilon}(t)$ is not easy to obtain. Assume that the unknown term $\tilde{\varepsilon}(t)$ is bounded as $|\tilde{\varepsilon}(t)| \le \eta$, where η is the positive unknown constant. Therefore, one proposes a novel adaptive parameter based on the barrier function $\hat{\eta}(t)$ to estimate the upper bound η of $|\tilde{\varepsilon}(t)|$ as follows:

$$\hat{\eta}(t) = \begin{cases} \hat{\eta}_A(t) & , \ if \ \ 0 < t \le t_r \\ \hat{\eta}_{PSD}(t) & , \ if \ \ t > t_r \end{cases} \tag{53}$$

where t_r is the time that the tracking error can converge to the neighborhood ι of the sliding manifold $\vartheta(t)$. Thus, the adaptation control gain and positive-semi-definite (PSD) barrier function can be formulated by (54) and (55), respectively, as:

$$\dot{\hat{\eta}}_A(t) = \mu|\vartheta(t)| \tag{54}$$

$$\hat{\eta}_{PSD}(t) = \frac{|\vartheta(t)|}{\iota - |\vartheta(t)|} \tag{55}$$

Then, the reaching control law $u^{re}_{TEC}(t)$ is determined as follows:

$$u^{re}_{TEC}(t) = -[\hat{\eta}(t) + \lambda]sgn(\vartheta(t)) \tag{56}$$

where λ is a positive constant.

From (52) and (56), the complete sub-control law $u_{TEC}(t)$ can be given as follows:

$$\begin{aligned} u_{TEC}(t) &= u^{eq}_{TEC}(t) + u^{re}_{TEC}(t) \\ &= \Big[-K_p x_1(t) - K_d x_2(t) + q_1 b_1 \mathcal{D}^{q_1+1}[sgn(x_1(t))^{a_1}] \\ &\quad + q_2 b_2 \mathcal{D}^{q_2}[sgn(x_1(t))^{a_2}] + \nu\sigma(0)exp(-\nu t) \\ &\quad - [\hat{\eta}(t) + \lambda]sgn(\vartheta(t))\Big] \end{aligned} \tag{57}$$

TABLE 5. Sensitivity analysis with proposed controller regarding settling time and peak undershoot.

Parameter	Change %	Settling time (s) for 5%band						Peak undershoot (-ve)(pu.Hz)					
		Δf_1	Δf_2	Δf_3	Δf_4	ΔP_{tie1}	ACE_1	Δf_1	Δf_2	Δf_3	Δf_4	$\Delta P_{tie,12}$	ACE_1
Nominal	0.0%	8.1829	11.1781	11.2087	11.2090	6.1123	8.0248	0.0065	0.0036	0.0036	0.0036	0.0041	0.0056
T_g	+50%	8.0050	10.9078	10.9315	10.9319	5.9905	5.8999	0.0072	0.0038	0.0038	0.0038	0.0043	0.0060
	+25%	8.0978	11.0538	11.0808	11.0811	6.0538	7.8135	0.0069	0.0037	0.0037	0.0037	0.0042	0.0058
	−25%	9.5194	11.2827	11.3154	11.3156	6.1645	8.1556	0.0062	0.0036	0.0035	0.0035	0.0040	0.0055
	−50%	9.9174	11.3673	11.4010	11.4012	6.2103	8.2512	0.0059	0.0035	0.0035	0.0035	0.0039	0.0054
T_t	+50%	7.7082	9.8362	10.0465	10.0468	5.8868	5.7760	0.0076	0.0043	0.0043	0.0043	0.0047	0.0066
	+25%	7.9207	10.6565	10.7341	10.7342	5.9834	5.8871	0.0071	0.0040	0.0039	0.0039	0.0044	0.0061
	−25%	10.0406	11.5772	11.6173	11.6174	6.2740	8.3829	0.0058	0.0033	0.0033	0.0033	0.0038	0.0052
	−50%	10.6186	11.8530	11.8919	11.8919	8.5263	8.6485	0.0050	0.0031	0.0031	0.0031	0.0036	0.0048
T_p	+50%	13.1935	14.4570	14.4263	14.4264	11.4586	11.3720	0.0058	0.0032	0.0032	0.0032	0.0044	0.0058
	+25%	10.5381	11.8731	11.8979	11.8980	8.6689	8.6736	0.0061	0.0034	0.0034	0.0034	0.0043	0.0057
	−25%	7.8121	10.4900	10.5865	10.5869	4.9999	4.8720	0.0072	0.0039	0.0038	0.0038	0.0038	0.0055
	−50%	6.8419	9.9979	10.1169	10.1178	5.0845	4.7904	0.0083	0.0041	0.0041	0.0041	0.0033	0.0054
K_p	+50%	7.6077	10.3112	10.4175	10.4180	4.9682	4.8271	0.0075	0.0040	0.0040	0.0039	0.0037	0.0054
	+25%	7.9451	10.6122	10.6963	10.6967	5.0205	4.8973	0.0070	0.0038	0.0038	0.0038	0.0038	0.0055
	−25%	10.7628	12.0581	12.0838	12.0838	9.7479	9.7479	0.0060	0.0033	0.0033	0.0033	0.0043	0.0058
	−50%	11.0941	14.4370	14.3938	14.3939	11.4663	11.3826	0.0055	0.0031	0.0031	0.0031	0.0042	0.0053

TABLE 6. Sensitivity analysis with proposed controller regarding IAE and ITAE indexes.

Parameter	Change %	IAE						ITAE					
		Δf_1	Δf_2	Δf_3	Δf_4	ΔP_{tie1}	ACE_1	Δf_1	Δf_2	Δf_3	Δf_4	$\Delta P_{tie,12}$	ACE_1
Nominal	0.0%	0.00840	0.00780	0.00780	0.00780	0.00521	0.00801	0.06377	0.06408	0.06453	0.06453	0.04467	0.06805
T_g	+50%	0.00865	0.09717	0.00794	0.00794	0.00515	0.00799	0.06317	0.06391	0.06441	0.06441	0.04422	0.06774
	+25%	0.00851	0.00789	0.00791	0.00791	0.00516	0.00801	0.06388	0.06397	0.06447	0.06447	0.04452	0.06789
	−25%	0.00838	0.00784	0.00787	0.00787	0.00530	0.00804	0.06377	0.06411	0.06460	0.06460	0.04558	0.06833
	−50%	0.00837	0.00782	0.00784	0.00784	0.00540	0.00808	0.06395	0.06418	0.06467	0.06467	0.04633	0.06871
T_t	+50%	0.00971	0.00807	0.00810	0.00810	0.00573	0.00821	0.06756	0.06394	0.06447	0.06447	0.04658	0.06815
	+25%	0.00901	0.00798	0.00801	0.00801	0.00540	0.00804	0.06542	0.06404	0.06454	0.06454	0.04545	0.06786
	−25%	0.00805	0.00775	0.00778	0.00778	0.00522	0.00802	0.06291	0.06406	0.06456	0.06456	0.04558	0.06852
	−50%	0.00795	0.00765	0.00767	0.00767	0.00549	0.00812	0.06322	0.06419	0.06467	0.06467	0.04824	0.06969
T_p	+50%	0.01148	0.00793	0.00791	0.00791	0.00953	0.01157	0.08361	0.06787	0.06784	0.06784	0.07768	0.09535
	+25%	0.00954	0.00786	0.00788	0.00788	0.00689	0.00895	0.06988	0.06542	0.06586	0.06586	0.05560	0.07383
	−25%	0.00795	0.00778	0.00781	0.00781	0.00450	0.00780	0.06107	0.06226	0.06280	0.06280	0.04120	0.06668
	−50%	0.00793	0.00760	0.00766	0.00766	0.00447	0.00767	0.05987	0.06016	0.06082	0.06082	0.04141	0.06590
K_p	+50%	0.00801	0.00780	0.00785	0.00785	0.00441	0.00771	0.06115	0.06210	0.06271	0.06271	0.04078	0.06636
	+25%	0.00800	0.00785	0.00788	0.00788	0.00455	0.08784	0.06165	0.06296	0.06352	0.06352	0.04146	0.06693
	−25%	0.00996	0.00779	0.00791	0.00791	0.00759	0.00957	0.07216	0.06537	0.06580	0.06580	0.06089	0.07826
	−50%	0.01077	0.00806	0.00806	0.00806	0.00822	0.01050	0.08057	0.06956	0.06956	0.06956	0.07149	0.08144

Finally, substituting (57) into (42), the control law of $\alpha(t)$-MF-ABFFONSMC is designed as below:

$$\begin{aligned} u(t) &= \frac{1}{\alpha(t)}\Big[q_1 b_1 \mathcal{D}^{q_1+1}[sgn(x_1(t))^{a_1}] + q_2 b_2 \mathcal{D}^{q_2}[sgn(x_1(t))^{a_2}] \\ &\quad + \nu\sigma(0)exp(-\nu t) - [\hat{\eta}(t)+\lambda]sgn(\vartheta(t)) + \ddot{y}(t) - \hat{\varepsilon}(t)\Big] \end{aligned} \tag{58}$$

To further improve the tracking performance of the proposed method, an $\alpha(t)$-variable approach is proposed to automatically update the value of α, and its corresponding formula is expressed as follows:

$$\dot{\alpha}(t) = -\Omega \mid \vartheta(t) \mid^{M} sgn(\alpha(t) - \alpha_{min}) \tag{59}$$

where α_{min} represents the positive lower bound of $\alpha(t)$, Ω and M are two positive designed parameters. Due to that $\alpha(t) = 0$ will cause the singularity in control input $u(t)$; therefore, the part of $sgn(\alpha(t) - \alpha_{min})$ is formulated to ensure that $\alpha(t)$ is not less than α_{min}.

C. STABILITY ANALYSIS OF $\alpha(T)$-MF-ABFFONSMC

Theorem 2: Consider the four-area interconnected hybrid power system (26) re-formulated by the ultra-local model (41), under the presented $\alpha(t)$-MF-ABFFONSMC (58), there exist appropriate coefficients q_1, q_2, b_1, b_2, a_1, a_2, ν, λ, Ω to ensure the stability of a closed-loop system and the convergence of tracking errors in finite time.

Proof: Substituting the control law (57) into (50) yields:

$$\dot{\vartheta}(t) = \kappa\left(-[\hat{\eta}(t)+\lambda]sgn(\vartheta(t)) + \tilde{\varepsilon}(t)\right) \tag{60}$$

For the proposed adaptive control gain $\hat{\eta}(t)$, there are two cases:

First case: For $0 < t \leq t_r$, let us select a Lyapunov function candidate as:

$$V(t) = \frac{1}{2}\vartheta^2(t) + \frac{\kappa}{2}\tilde{\eta}_A^2 + \frac{1}{2}\tilde{\alpha}^2(t) \tag{61}$$

with $\tilde{\eta}_A = \hat{\eta}_A - \eta_A$ and $\tilde{\alpha}(t) = \alpha(t) - \alpha_{min}$.

Differentiating $V(t)$ and using (54), one can obtain the following form:

$$\begin{aligned} \dot{V}(t) &= \vartheta(t)\dot{\vartheta}(t) + \kappa\tilde{\eta}_A\dot{\tilde{\eta}}_A + \tilde{\alpha}(t)\dot{\alpha}(t) \\ &= \kappa\vartheta(t)\left(-[\hat{\eta}_A(t)+\lambda]sgn(\vartheta(t)) + \tilde{\varepsilon}(t)\right) \\ &\quad + \kappa\mu(\hat{\eta}_A - \eta_A)|\vartheta(t)| - \Omega|\vartheta(t)|^{M}|\tilde{\alpha}(t)| \\ &\leq \kappa|\vartheta(t)||\tilde{\varepsilon}(t)| - \kappa\hat{\eta}_A(t)|\vartheta(t)| - \kappa\lambda|\vartheta(t)| \\ &\quad + \kappa\mu|\vartheta(t)|(\hat{\eta}_A - \eta_A)|\vartheta(t)| - \Omega \mid \vartheta(t) \mid^{M} |\tilde{\alpha}(t)| \end{aligned} \tag{62}$$

TABLE 7. Performance of proposed controller against RLP in terms of IAE and TAE indexes.

Controller	IAE						ITAE					
	Δf_1	Δf_2	Δf_3	Δf_4	ΔP_{tie1}	ACE_1	Δf_1	Δf_2	Δf_3	Δf_4	$\Delta P_{tie,12}$	ACE_1
IPSO: FOPID [15]	0.1782	0.1716	0.1717	0.1717	0.1020	0.1748	12.71	12.2	12.2	12.2	7.325	12.48
MPA: SMDO-iPD	0.1685	0.1477	0.1478	0.1478	0.1068	0.1608	11.02	10.46	10.46	10.46	6.622	11.44
ALO: PID+DD [14]	0.137	0.1194	0.1197	0.1197	0.08667	0.1300	9.5	8.233	8.237	8.237	6.118	9.041
IGWO: Fuzzy-PID [22]	0.1615	0.1527	0.1537	0.1537	0.0968	0.1602	11.07	10.47	10.55	10.55	6.814	11.08
hFPAPFA: FOSWPID [16]	0.0621	0.0586	0.0585	0.0585	0.03704	0.0593	4.232	4.038	4.036	4.036	2.486	4.03
MPA: MF-ABFFONSMC	0.0277	0.0275	0.0275	0.0275	0.0150	0.0245	1.891	1.894	1.894	1.894	1.007	1.661
MPA: $\alpha(t)$-MF-ABFFONSMC	0.0134	0.0127	0.0126	0.0126	0.0098	0.0134	0.911	0.872	0.864	0.864	0.662	0.9031

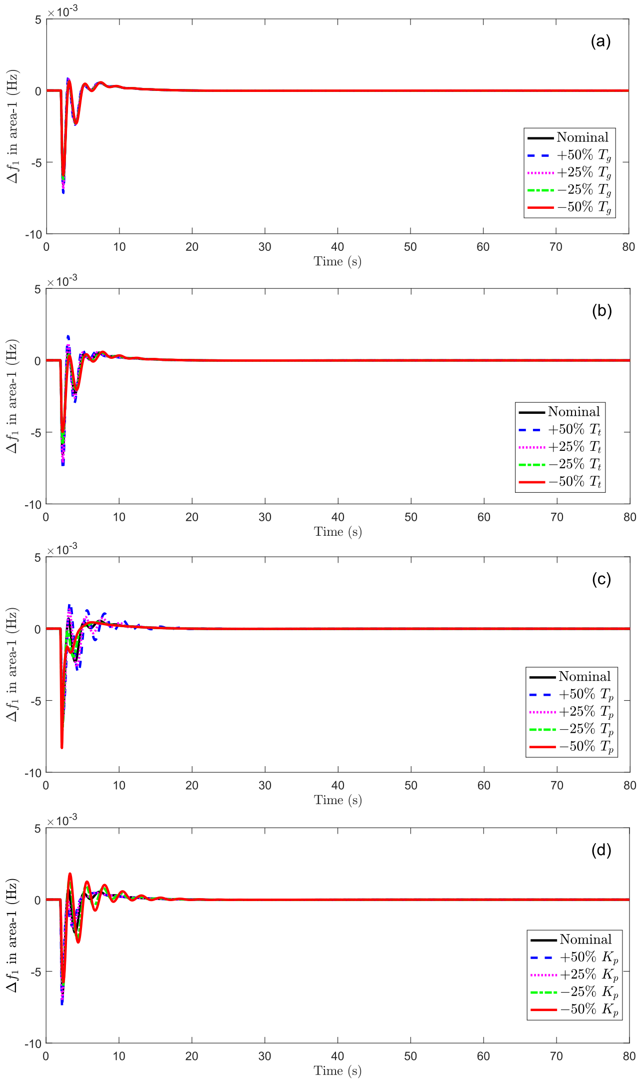

FIGURE 13. The sensitivity analysis using the proposed controller (frequency deviation in area−1 Δf_1, under applied 1%step load disturbance):(a) Uncertainty in T_g, (b) Uncertainty in T_t, (c) Uncertainty in T_p, and (d) Uncertainty in K_p.

By adding $+\varpi|\vartheta(t)|\eta_A$ and $-\varpi|\vartheta(t)|\eta_A$ for the left side of (62), it yields:

$$\begin{aligned}\dot{V}(t) &\leq \kappa|\vartheta(t)||\tilde{\varepsilon}(t)| - \kappa\hat{\eta}_A(t)|\vartheta(t)| \\ &\quad + \kappa\mu|\vartheta(t)|(\hat{\eta}_A - \eta_A) + \kappa|\vartheta(t)|\eta_A \\ &\quad - \kappa|\vartheta(t)|\eta_A - \Omega \mid \vartheta(t) \mid^M |\tilde{\alpha}(t)| \\ &\leq -\kappa|\vartheta(t)|(\eta_A - |\tilde{\varepsilon}(t)|) - \kappa\lambda|\vartheta(t)| - \kappa(1-\mu) \\ &\quad \times (\hat{\eta}_A - \eta_A)|\vartheta(t)| - \Omega \mid \vartheta(t) \mid^M |\tilde{\alpha}(t)| \end{aligned} \tag{63}$$

Since $\eta_A > |\tilde{\varepsilon}(t)|$ and $0 < \mu < 1$, therefore (63) can be reformulated as follows:

$$\begin{aligned}&\dot{V}(t) \\ &\leq -\sqrt{2}\kappa(\eta_A - |\tilde{\varepsilon}(t)| + \lambda)\frac{|\vartheta(t)|}{\sqrt{2}} - \sqrt{2\kappa}(1-\mu)\frac{\tilde{\eta}_A}{\sqrt{\frac{2}{\kappa}}}|\vartheta(t)| \\ &\quad - \sqrt{2}\Omega \mid \vartheta(t) \mid^M |\tilde{\alpha}(t)| \end{aligned} \tag{64}$$

According to the widely accepted inequality $\sqrt{x^2+y^2+z^2} \leq |x|+|y|+|z|$, $\dot{V}(t)$ in (65) can be derived as:

$$\begin{aligned}\dot{V}(t) &\leq -min\left\{\sqrt{2}\kappa(\eta_A - |\tilde{\varepsilon}(t)| + \lambda), \sqrt{2\kappa}(1-\mu)|\vartheta(t)|,\right. \\ &\quad \left.\sqrt{2}\Omega \mid \vartheta(t) \mid^M\right\}\left(\frac{|\vartheta(t)|}{\sqrt{2}} + \frac{|\tilde{\eta}_A|}{\sqrt{\frac{2}{\kappa}}} + \frac{|\tilde{\alpha}(t)|}{\sqrt{2}}\right) \\ &\leq -\aleph V^{\frac{1}{2}}(t) \end{aligned} \tag{65}$$

where $\aleph = min\left\{\sqrt{2}\kappa(\eta_A - |\tilde{\varepsilon}(t)| + \lambda), \sqrt{2\kappa}(1-\mu)\right.$ $\left.|\vartheta(t)|, \sqrt{2}\Omega \mid \vartheta(t) \mid^M\right\}\rangle 0$. Thus, it is clear from (65) that by using the adaptive law (54), the fractional order nonlinear sliding surface will converge to zero in finite time.

Second case: For $t > t_r$, the Lyapunov function candidate is defined as follows:

$$\Gamma(t) = \frac{1}{2}\vartheta^2(t) + \frac{1}{2}\hat{\eta}_{PSD}^2 + \frac{1}{2}\tilde{\alpha}^2(t) \tag{66}$$

The first time derivative of (66) is given as:

$$\dot{\Gamma}(t) = \vartheta(t)\dot{\vartheta}(t) + \hat{\eta}_{PSD}(t)\dot{\hat{\eta}}_{PSD}(t) + \tilde{\alpha}(t)\dot{\alpha}(t) \tag{67}$$

By substituting $\dot{\vartheta}(t)$ (50), (55) into (67), one can get:

$$\begin{aligned}&\dot{\Gamma}(t) \\ &= \kappa\vartheta(t)\left\{-[\hat{\eta}_{PSD}(t) + \lambda]sgn(\vartheta(t)) + \tilde{\varepsilon}(t)\right\} \\ &\quad + \hat{\eta}_{PSD}(t)\dot{\hat{\eta}}_{PSD}(t) - \Omega|\vartheta(t)|^M|\tilde{\alpha}(t)| \\ &\leq -\kappa\left\{\hat{\eta}_{PSD}(t) - |\tilde{\varepsilon}(t)| + \lambda\right\}|\vartheta(t)| + \hat{\eta}_{PSD}(t)\frac{\iota}{(\iota - |\vartheta(t)|)^2} \\ &\quad \times sgn(\vartheta(t))\dot{\vartheta}(t) - \Omega|\vartheta(t)|^M|\tilde{\alpha}(t)| \\ &\leq -\kappa\left\{\hat{\eta}_{PSD}(t) - |\tilde{\varepsilon}(t)| + \lambda\right\}|\vartheta(t)| + \kappa\hat{\eta}_{PSD}(t) \\ &\quad \times \frac{\iota}{(\iota - |\vartheta(t)|)^2}\left\{\tilde{\varepsilon}(t) - [\hat{\eta}_{PSD}(t) + \lambda]sgn(\vartheta(t))\right\}sgn(\vartheta(t)) \\ &\quad - \Omega|\vartheta(t)|^M|\tilde{\alpha}(t)| \end{aligned} \tag{68}$$

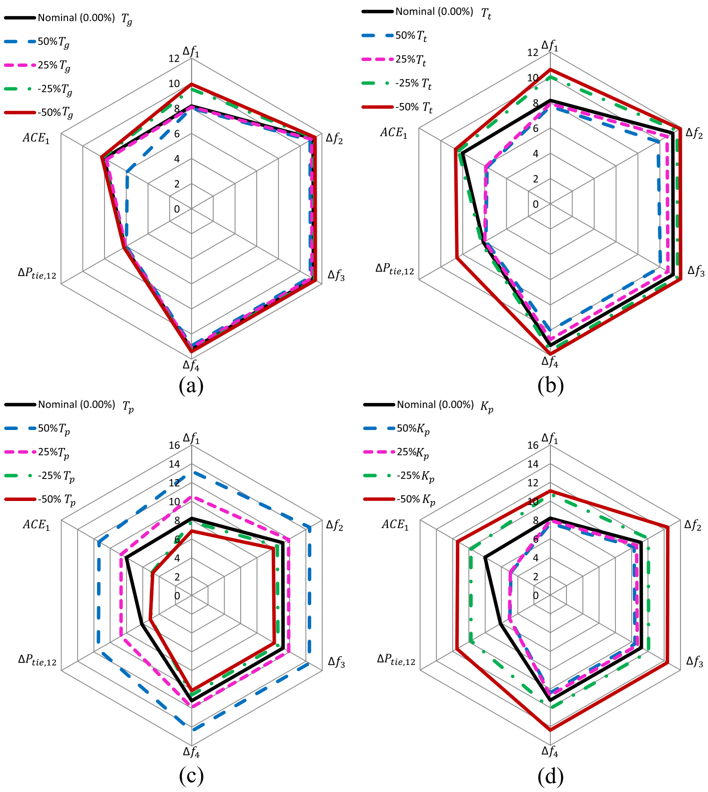

FIGURE 14. The graphical representation of settling time:(a) Uncertainty in T_g, (b) Uncertainty in T_t, (c) Uncertainty in T_p, and (d) Uncertainty in K_p.

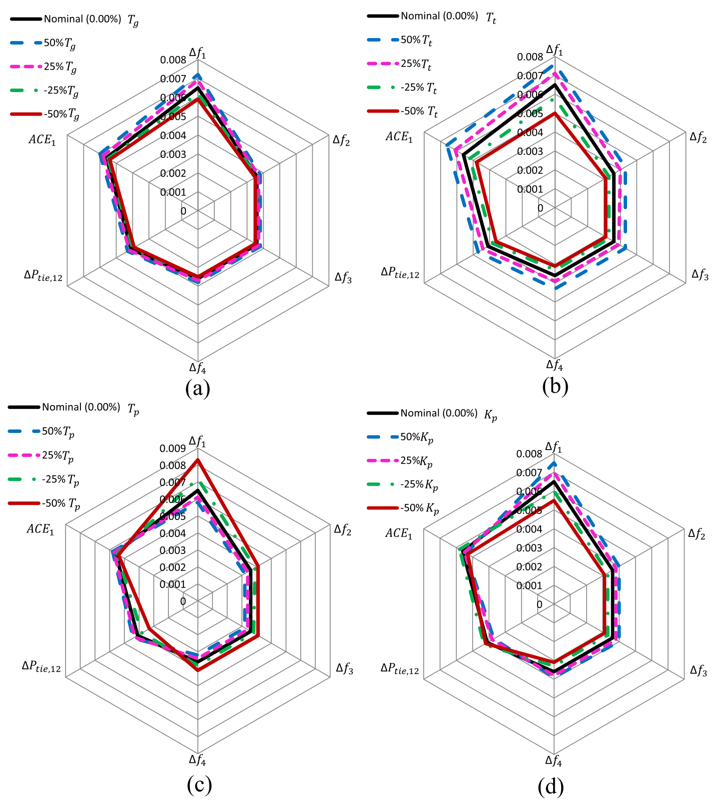

FIGURE 15. The graphical representation of peak undershoot:(a) Uncertainty in T_g, (b) Uncertainty in T_t, (c) Uncertainty in T_p, and (d) Uncertainty in K_p.

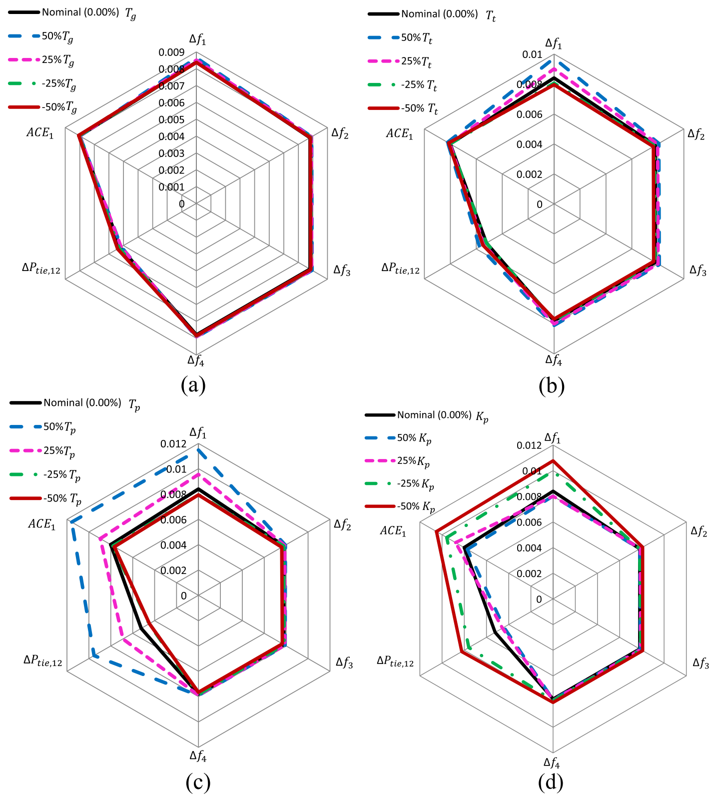

FIGURE 16. The graphical representation of IAE:(a) Uncertainty in T_g, (b) Uncertainty in T_t, (c) Uncertainty in T_p, and (d) Uncertainty in K_p.

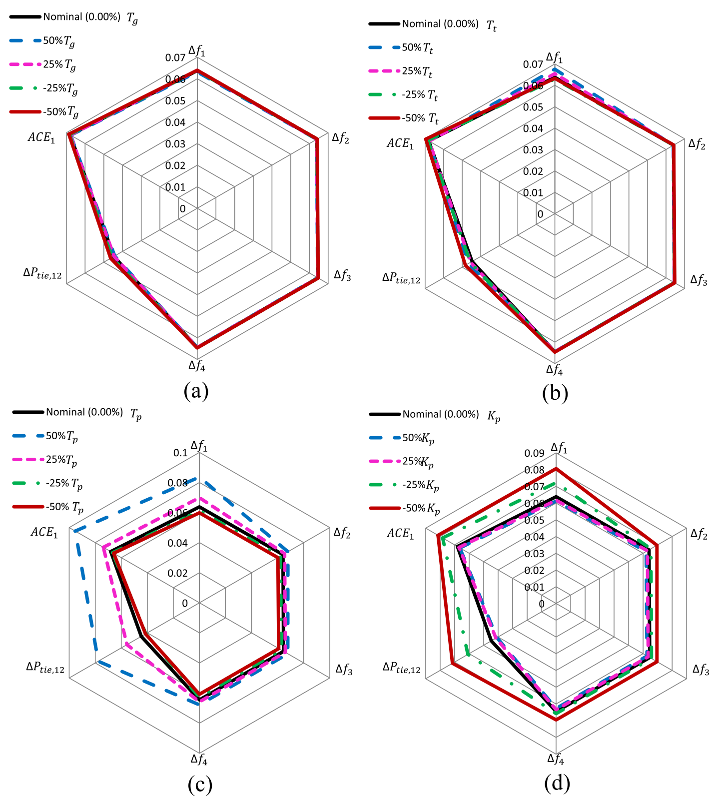

FIGURE 17. The graphical representation of ITAE:(a) Uncertainty in T_g, (b) Uncertainty in T_t, (c) Uncertainty in T_p, and (d) Uncertainty in K_p.

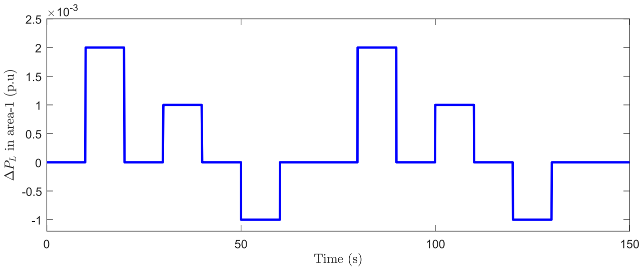

FIGURE 18. The random loading perturbation (RLP).

Then, (68) can be rewritten as:

$$\dot{\Gamma}(t) \leq -\kappa\left\{\hat{\eta}_{PSD}(t)-|\tilde{\varepsilon}(t)|+\lambda\right\}|\vartheta(t)|-\kappa\hat{\eta}_{PSD}(t) \times\frac{\iota}{(\iota-|\vartheta(t)|)^2}\left\{\hat{\eta}_{PSD}(t)-|\tilde{\varepsilon}(t)|+\lambda\right\}-\Omega|\vartheta(t)|^M|\tilde{\alpha}(t)| \tag{69}$$

Because $\hat{\eta}_{PSD}(t) \geq |\tilde{\varepsilon}(t)|$, $\lambda > 0$ and $\frac{\iota}{(\iota-|\vartheta(t)|)^2} > 0$, one has:

$$\dot{\Gamma}(t) \leq -\sqrt{2}\kappa\left\{\hat{\eta}_{PSD}(t)-|\tilde{\varepsilon}(t)|+\lambda\right\}\frac{|\vartheta(t)|}{\sqrt{2}}-\frac{\sqrt{2}\kappa\iota}{(\iota-|\vartheta(t)|)^2} \times\left\{\hat{\eta}_{PSD}(t)-|\tilde{\varepsilon}(t)|+\lambda\right\}\frac{\hat{\eta}_{PSD}(t)}{\sqrt{2}}-\sqrt{2}\Omega|\vartheta(t)|^M|\tilde{\alpha}(t)|$$

$$\dot{\Gamma}(t) \leq -\Im\left[\frac{|\vartheta(t)|}{\sqrt{2}}+\frac{\hat{\eta}_{PSD}(t)}{\sqrt{2}}+\frac{|\tilde{\alpha}(t)|}{\sqrt{2}}\right]$$

$$\dot{\Gamma}(t) \leq -\Im\Gamma^{\frac{1}{2}}(t) \tag{70}$$

where $\Im = \sqrt{2}min\left(\kappa\left\{\hat{\eta}_{PSD}(t)-|\tilde{\varepsilon}(t)|+\lambda\right\}, \frac{\iota\kappa\left\{\hat{\eta}_{PSD}(t)-|\tilde{\varepsilon}(t)|+\lambda\right\}}{(\iota-|\vartheta(t)|)^2}, \Omega|\vartheta(t)|^M\right)$. □

D. THE OBJECTIVE FUNCTION AND MPA-BASED PARAMETER OPTIMIZER DESIGN

Reconstructing the fundamental capability of frequency regulation, returning the frequency to the intended value as fast as possible, and reducing power flow deviations between interconnected control areas are the goals of the controller design for four-area interconnected hybrid power systems. Hence, to achieve the aforementioned goals, the parameters of the proposed $\alpha(t)$-MF-ABFFONSMC should be optimized to get fast settling time and minimum peak overshot in area frequency and tie-line power flow. The performance index that is typically considered for designing a controller is an integral time-weighted absolute error (ITAE). The expression of ITAE is given as:

$$J = ITAE = \int t.(|\Delta f_1|+|\Delta f_2|+|\Delta f_3|+|\Delta f_4|+|\Delta P_{tie,12}|)dt \tag{71}$$

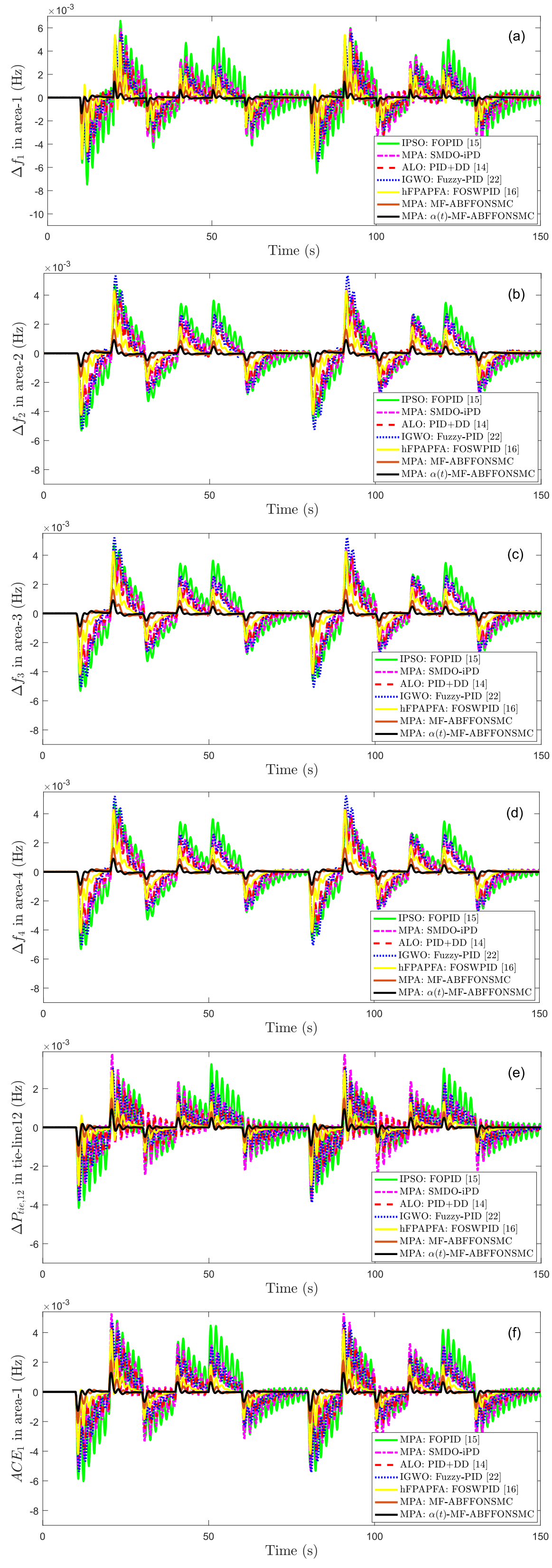

FIGURE 19. Performance of proposed controller against RLP:(a),(b),(c) and (d) show frequency deviations in a four area,(e) represents the power deviation in tie-line−12 $\Delta P_{tie,12}$, and (f) displays the ACE deviation in area−1.

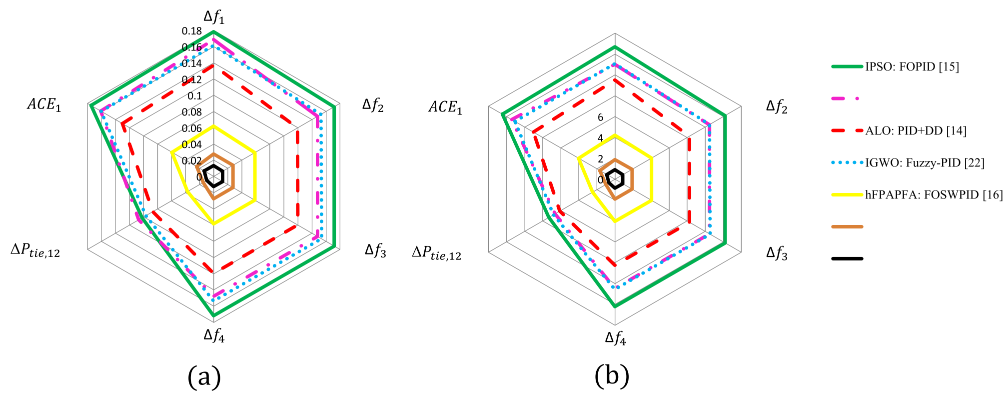

FIGURE 20. The graphical representation of IAE and ITAE indexes for performance of proposed controller against RLP:(a) IAE and (b) ITAE.

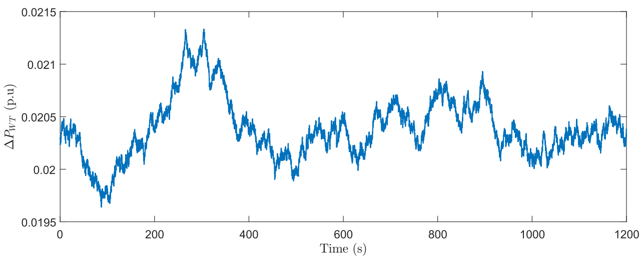

FIGURE 21. The wind turbine power fluctuation.

In order to provide optimal control performance, the optimizer parameter based on MPA is adjusted to get the optimal parameters q_1^*, q_2^*, b_1^*, b_2^*, a_1^*, a_2^*, ν^*, λ^*, Ω^* of the $\alpha(t)$-MF-ABFFONSMC.

The MPA is a newly developed metaheuristic approach that draws inspiration from the natural movements observed in ocean predators, specifically the Lévy and Brownian motions. Additionally, it incorporates the concept of the optimum encounter rate policy observed in biological interactions between predator and prey.

In this paper, every prey is expressed as a vector with dimension (1×9), and then M preys establish a matrix Prey $\in \mathbb{R}^{M\times 9}$. For the selection of the top predator from the prey, the fitness function J defined in (71) is used to evaluate each prey. Moreover, the determined top predator is reproduced N times to form a matrix Elite $\in \mathbb{R}^{M\times 9}$. The optimization process of the MPA can be categorized into three stages:

Stage A: In this stage, the predator is moving slower than the prey in the initial iterations of optimization.

The exploration rule governing prey with Brownian motion can be expressed as:

$$\begin{aligned} &While < \frac{1}{3} Iter_{Max} \\ &\quad H_j = \bar{R}_b \odot (Elite_i - \bar{R}_b \odot Prey_j) \\ &\quad Prey_j = Prey_j + \bar{P}\bar{R} \odot H_j, \quad with \;\; j = 1, 2, \ldots, M \end{aligned} \tag{72}$$

where k, $Iter_{Max}$, and H_j are the current iteration, the maximum iteration, and the iteration step size, respectively. $\odot$ is entry-wise multiplication, $\bar{R}_b^{1\times 9}$ represents a vector containing the normal random distribution numbers of Brownian motion, and P is a positive constant. $\bar{R}^{1\times 9}$ denotes a vector of uniform random numbers with a range between 0 and 1. $Prey_j$ is the j^{th} row vector in the prey matrix, and $Elite_j$ is the j^{th} row vector in the prey matrix.

Stage B: In the middle stage, the predator and prey are both moving at the same speed. Therefore, the prey is responsible for exploitation using Lévy motion, whereas the predator is responsible for exploration using Brownian motion.

$$\begin{aligned} &While \frac{1}{3} Iter_{Max} < k < \frac{2}{3} Iter_{Max} \\ &\quad H_j = \bar{R}_l \odot (Elite_j - \bar{R}_l \odot Prey_j) \\ &\quad Prey_j = Prey_j + \bar{P}\bar{R} \odot H_j, \quad with \;\; j = 1, 2, \ldots, M/2 \\ &\quad H_j = \bar{R}_l \odot (R_b \odot Elite_j - Prey_j) \\ &\quad Elite_j = Elite_j + \bar{P}C \odot H_j, \quad with \;\; j = M/2, \ldots, M \end{aligned} \tag{73}$$

where $\bar{R}_l^{1\times 9}$ represents a vector containing random distribution numbers of Lévy motion and $C = (1 - \frac{k}{Iter_{Max}})^{\frac{2k}{Iter_{Max}}}$ denotes an adaptive parameter.

Stage C: In the last stage, the predator is moving faster than the prey, and then the best strategy for the predator is exploitation with Lévy and its description can be given as follows:

$$\begin{aligned} &While > \frac{2}{3} Iter_{Max} \\ &\quad H_j = \bar{R}_l \odot (R_l \odot Elite_j - Prey_j) \\ &\quad Prey_j = Elite_j + \bar{P}C \odot H_j, \quad with \;\; j = 1, 2, \ldots, M \end{aligned} \tag{74}$$

Then, for the avoidance of trapping in a local optima, fish aggregating devices (FADs) or the eddy formation effects are utilized.

$$Prey_j = \begin{cases} Prey_j + C \odot (Z_{min} +) R \odot (Z_{max} - Z_{min}) \odot U, & l \le \chi \\ Prey_j + (\chi(1-l) + l)(Prey_{l_1} - Prey_{l_2}), & l > \chi \end{cases} \tag{75}$$

TABLE 8. Performance of proposed controller against wind speed fluctuations in terms of IAE and TAE indexes.

Controller	IAE						ITAE					
	Δf_1	Δf_2	Δf_3	Δf_4	ΔP_{tie1}	ACE_1	Δf_1	Δf_2	Δf_3	Δf_4	$\Delta P_{tie,12}$	ACE_1
IPSO: FOPID [15]	0.7207	0.4629	0.4136	0.4136	0.4214	0.5832	110.5	92.47	90.69	90.69	81.07	116.4
MPA: SMDO-iPD	0.3792	0.3209	0.3208	0.3208	0.3208	0.3297	80.14	70.74	70.74	70.75	58.94	85.63
ALO: PID+DD [14]	0.4362	0.3878	0.3915	0.3915	0.2334	0.3631	90.36	83.48	83.52	83.52	68.60	99.32
IGWO: Fuzzy-PID [22]	0.3190	0.3055	0.3065	0.3065	0.1716	0.2742	84.19	82.86	82.60	82.60	58.32	88.71
hFPAPFA: FOSWPID [16]	0.236	0.1612	0.1606	0.1606	0.1517	0.2025	34.55	40.74	40.72	40.72	27.36	40.19
MPA: MF-ABFFONSMC	0.0817	0.0670	0.0670	0.0670	0.0528	0.0748	26.23	26.56	26.56	26.56	19.93	28.84
MPA: $\alpha(t)$-MF-ABFFONSMC	0.0084	0.0078	0.0078	0.0078	0.0078	0.0080	0.063	0.064	0.064	0.064	0.044	0.068

where $Z_{min} \in \mathbb{R}^{1\times 9}$ and $Z_{max} \in \mathbb{R}^{1\times 9}$ represent lower and upper bounds vectors. $U \in \mathbb{R}^{1\times 9}$ denotes the binary vector including zero and one. χ denotes a positive constant that influences the optimization process; l is the uniform random number within the range of [0, 1); l_1 and l_2 are the random indexes of the prey matrix.

IV. SIMULATION RESULTS AND DISCUSSION

In order to validate the performance of the proposed controller as an efficient control technique for the LFC problem, four-area interconnected hybrid power systems are considered for the current work in Fig. 6. In addition, boiler dynamics and physical constraints are considered and incorporated into the reheat thermal power system. The models of the considered hybrid power systems are performed in MATLAB/SIMULINK environment. The hybrid power system's parameters used in the simulation are listed in Table 1. The wind turbine-based LFC is located in every area with a constant speed of 12 m/s to provide active power that supports the network frequency. The filter order and the lower/upper-frequency parameters in the fractional order control (FOC) are taken as 5 and [0.001; 1000] Hz, respectively. In addition, the corresponding simulation results of the MPA-optimized $\alpha(t)$-MF-ABFFONSMC technique are compared with those of other approaches such as PSO-optimized fractional-order PID controller (FOPID) [15], SMDO-iPD, ALO-optimized PID+DD [14], IGWO-optimized fuzzy PID controller [22], and hFPAPFA-optimized FOSWPID [16]. The optimal controller parameters obtained for 80 iterations using the MPA algorithm and the controller parameters proposed in PSO-optimized FOPID [15], ALO-optimized PID+DD [14], IGWO-optimized fuzzy PID [22] and hFPAPFA-optimized FOSWPID [16] are given in Table 2. The fitness function convergences of the different optimization techniques is shown in Fig. 8. The following three scenarios are considered in this paper for the assessment of the proposed controller:

A. CASE 1. PERFORMANCE EVALUATION OF THE INTERCONNECTED HYBRID POWER SYSTEM WITH NONLINEARITIES AND CONSTANT WIND SPEED

1) FIRST SCENARIO

In this scenario, the simulation was carried out using the nominal parameters of the hybrid power system as listed in Table 1, in the presence of the nonlinearity effects in all areas and step load disturbance 1% in area−1. The dynamic performance of the proposed controller with the other approaches is shown in Fig. 9. The findings from the upper to the bottom, which are shown in Fig. 9, are frequency deviations in areas (1−4), power deviation of tie-line−12 and control error in area−1 ACE_1. The control inputs of all areas are depicted in Fig. 10. The updating curve of $\alpha(t)$ of $\alpha(t)$-MF-ABFFONSMC is shown in Fig. 11. Furthermore, to assess the output response of the proposed strategy compared to the other methods, performance indicators such as integral absolute error (IAE), integral time absolute error (ITAE), settling time, and peak undershoots are used in this paper. The dynamic response of the proposed method concerning peak undershoots and settling time for the 5% band is displayed in Table 3. In addition, the numerical values of the IAE and ITAE indexes are furnished in Table 4. Corresponding graphical representations of settling time, peak undershoots, IAE, and ITAE are shown in Fig. 12(a), Fig. 12(b), Fig. 12(c), and Fig. 12(d), respectively. The results presented in Fig. 9 demonstrate that the oscillations of the transient responses with the proposed controller converge to the steady state value faster than the other approaches. Moreover, it is visualized from Tables 3 and 4 that better settling time and peak undershoot with minimum values of IAE and ITAE indexes of the system responses are acquired by the proposed controller than the other compared techniques. Consequently, the dynamic performance of the proposed controller exhibits greater advantages compared to other controllers and appears to meet the requirements of load frequency control (LFC) even in the presence of boiler dynamics and physical constraints.

2) SECOND SCENARIO: SENSITIVITY ANALYSIS

In this scenario, the dynamic performance of the proposed method is assessed with a wide variation of system parameters and loading conditions in the presence of boiler dynamics and physical constraints. In order to carry out this test, the step load disturbance 1% in area−1 and some parameters of the power system like T_g, T_t, T_p, and K_p are varied around their nominal values in the range from +50% to −50% in steps of 25%, i.e., $T_g \in [0.5T_g, 0.75T_g, 1.25T_g, 1.5T_g]$, $T_t \in [0.5T_t, 0.75T_t, 1.25T_t, 1.5T_t]$, $T_p \in [0.5T_p, 0.75T_p, 1.25T_p, 1.5T_p]$, $K_p \in [0.5K_p, 0.75K_p, 1.25K_p, 1.5K_p]$. The frequency deviations in area−1 Δf_1 under applied step load disturbance 1% in area−1 with the uncertainties in parameters T_g, T_t, T_p and K_p) are illustrated in Fig. 13(a), 13(b), 13(c), and 13(d), respectively. The corresponding quantitative analysis in terms of performance indexes (settling time, peak undershoot, IAE, and ITAE) is summarized in Tables 5 and 6. Figures 14(a), 14(b), 14(c), and 14(d) present the graphical representation of settling time for uncertainties in parameters T_g, T_t, T_p, and K_p, respectively, while the graphical representation of peak undershoot for uncertainties in parameters T_g, T_t, T_p, and K_p are depicted in Figs. 15(a), 15(b), 15(c), and 15(d), respectively. Furthermore, the graphical representation of IAE for uncertainties in parameters T_g, T_t, T_p, and K_p is illustrated in Figs. 16(a), 16(b), 16(c), and 16(d), respectively, while the graphical representation of ITAE for uncertainties in parameters T_g, T_t, T_p, and K_p are shown in Figs. 15(a), 17(b), 17(c), and 17(d), respectively. The results shown in Fig. 13 and quantitative analysis of performance indexes are displayed in Tables 5, 6 and Figs. 14, 15, 16, and 17 indicate that there is minimal variation in system performance when the loading condition and plant's parameters are changed by $\pm 50\%$ from their designated values. Thus, it can be deduced that the suggested control method provides robust and reliable control, and the controller parameters achieved under loading conditions with nominal parameters do not require adjustment for significant variations in system parameters or system loading.

3) THIRD SCENARIO: PERFORMANCE OF PROPOSED CONTROLLER AGAINST RANDOM LOADING PERTURBATION (RLP)

To further analyze the robustness of the proposed method against the random nature of the load, RLP, as illustrated in Fig. 18, is considered and applied in area-1 at 2s as a disturbance, using the same optimal values of the proposed controller parameters that were obtained in the first scenario. The RLP is random both in duration and magnitude [22]. The dynamic performance of the considered hybrid power system concerning frequency deviations in areas $(1-4)(\Delta f_1,\ \Delta f_2,\ \Delta f_3,\ \Delta f_4)$, power deviation of tie-line-12 ΔP_{tie1} and control error in area-1 ACE_1 are shown in Fig. 19. The corresponding quantitative analysis in terms of performance indexes (IAE, ITAE) is furnished in Table 7, and their corresponding graphical representations are displayed in Fig. 20. It is obliviously seen from Figs. 19, 20 and Table 7 that the proposed controller provides a better transient response with minimum performance indexes against RLP in the existence of boiler dynamics and physical constraints.

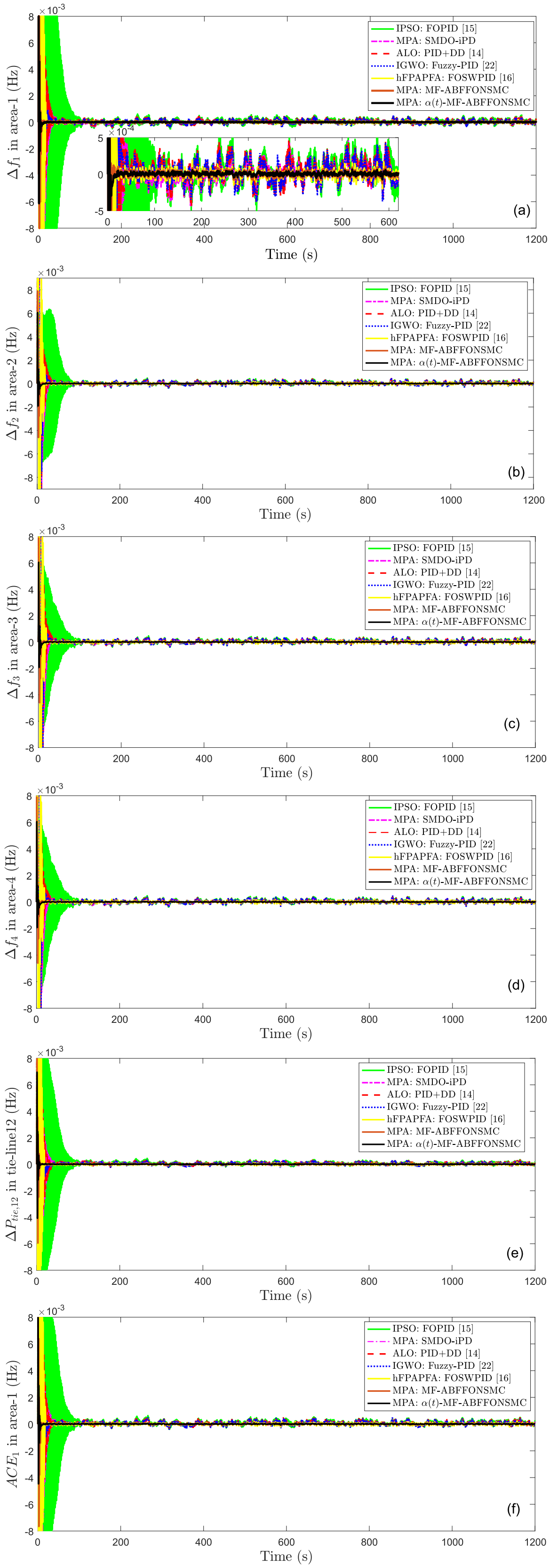

FIGURE 22. Performance of proposed controller against wind speed fluctuations:(a),(b),(c) and (d) show frequency deviations in a four area,(e) represents the power deviation in tie-line-12 $\Delta P_{tie,12}$, and (f) displays the ACE deviation in area-1.

B. CASE 2. PERFORMANCE EVALUATION OF THE INTERCONNECTED HYBRID POWER SYSTEM WITH WIND POWER FLUCTUATION

In this case, the frequency stabilization of the four-area interconnected power system comprising wind turbines is simulated and confirmed under wind speed fluctuations to validate the control performance of the proposed method. The dynamic performance of the proposed method is tested at nominal parameters by applying the step load disturbance 1% in area-1 and wind speed fluctuations for all areas.

The applied wind turbine power fluctuation for all areas is shown in Fig. 21. The corresponding dynamic performance curves for the area frequency, tie-line power, and control error deviations in area−1 are depicted in Fig. 22. The quantitative analysis in terms of performance indexes (IAE, ITAE) is listed in Table 8. It is observed from Fig. 22 and Table 8 that the dynamic performance of the proposed methods is much better than the other methods, as indicated by the variation curves of area frequency, tie-line power, and ACE deviations under wind speed fluctuations.

V. CONCLUSION

For the load frequency control (LFC) problem of a four-area interconnected hybrid power system with boiler dynamics, physical constraints, and load disturbance, a robust α-variable model-free adaptive barrier-function fractional-order nonlinear sliding mode control ($\alpha(t)$-MF-ABFFONSMC) is proposed in this article. This presented $\alpha(t)$-MF-ABFFONSMC can provide good control performance with high precision and fast response speed under loading conditions. From the obtained simulation results on a four-area interconnected hybrid power system, the MF-ABFFONSMC has strong robustness against nonlinearities due to physical constraints and boiler dynamics. The performance indexes in terms of settling time with the proposed MPA-tuned $\alpha(t)$-MF-ABFFONSMC controller is improved about 23% over MPA-tuned MF-ABFFONSMC, 41% over hFPAPFA-tuned FOSWPID, 55% over IGWO-tuned Fuzzy-PID, 58% over ALO-tuned PID+DD, 64% over MPA-tuned SMDO-iPD, and 72% over IPSO-tuned FOPID. Furthermore, it can be concluded that the proposed approach achieves stable and robust control, satisfying the gains of the proposed $\alpha(t)$-MF-ABFFONSMC, and there is no need for a reset even if the system is tested under a wide variation in the system's parameters and loading conditions.

In this current work, we only validated the proposed method using Matlab/Simulink, therefore, it is crucial to provide any limitations or constraints that may exist through an experimental test. This opens up opportunities for future research and improvement, as well as fosters a deeper understanding of the potential challenges that may arise when applying the method in practical settings.

Moreover, in future work, the effect of three-phase short circuits and similar faults in multi-area interconnected hybrid power systems will be studied and investigated.

ACKNOWLEDGMENT

The authors would like to acknowledge the support of the Tertiary Education Scientific Research Project of Guangzhou Municipal Education Bureau and the Researchers Supporting Project of King Saud University.

REFERENCES

[1] P. Kundur, *Power System Stability and Control*. New York, NY, USA: McGraw-Hill, 1994.

[2] B. Mohanty, S. Panda, and P. K. Hota, "Controller parameters tuning of differential evolution algorithm and its application to load frequency control of multi-source power system," *Int. J. Electr. Power Energy Syst.*, vol. 54, pp. 77–85, Jan. 2014.

[3] N. V. Kumar and M. M. T. Ansari, "A new design of dual-mode type-II fuzzy logic load frequency controller for interconnected power systems with parallel AC–DC tie-lines and superconducting magnetic energy storage unit," *Energy*, vol. 89, pp. 37–118, Sep. 2015.

[4] K. Vrdoljak, N. Perić, and I. Petrović, "Sliding mode based load-frequency control in power systems," *Electr. Power Syst. Res.*, vol. 80, no. 5, pp. 514–527, May 2010.

[5] R. K. Sahu, S. Panda, and N. K. A. Yegireddy, "A novel hybrid DEPS optimized fuzzy PI/PID controller for load frequency control of multi-area interconnected power systems," *J. Process Control*, vol. 24, no. 10, pp. 608–1596, 2014.

[6] S. Subha, "Load frequency control with fuzzy logic controller considering governor dead band and generation rate constraint nonlinearities," *World Appl. Sci. J.*, vol. 29, no. 8, pp. 1059–1066, 2014.

[7] Y. Sun, N. Li, X. Zhao, Z. Wei, G. Sun, and C. Huang, "Robust H_∞ load frequency control of delayed multi-area power system with stochastic disturbances," *Neurocomputing*, vol. 193, pp. 58–67, Jun. 2016.

[8] A. H. G. Haroun and Y.-Y. Li, "Ant lion optimized fractional order fuzzy pre-compensated intelligent pid controller for frequency stabilization of interconnected multi-area power systems," *Appl. Syst. Innov.*, vol. 2, no. 2, p. 17, May 2019.

[9] Y. Mi, X. Hao, Y. Liu, Y. Fu, C. Wang, P. Wang, and P. C. Loh, "Sliding mode load frequency control for multi-area time-delay power system with wind power integration," *IET Gener., Transmiss. Distrib.*, vol. 11, no. 18, pp. 4644–4653, Dec. 2017.

[10] N. Vafamand, M. M. Arefi, M. H. Asemani, and T. Dragicevic, "Decentralized robust disturbance-observer based LFC of interconnected systems," *IEEE Trans. Ind. Electron.*, vol. 69, no. 5, pp. 4814–4823, May 2022.

[11] W. Fan, Z. Hu, and V. Veerasamy, "PSO-based model predictive control for load frequency regulation with wind turbines," *Energies*, vol. 15, no. 21, p. 8219, Nov. 2022.

[12] S. Ekinci, Ö. Can, M. S. Ayas, D. Izci, M. Salman, and M. Rashdan, "Automatic generation control of a hybrid PV-reheat thermal power system using RIME algorithm," *IEEE Access*, vol. 12, pp. 26919–26930, 2024.

[13] J. Mao, R. Liu, A. Wu, S. Wu, and J. He, "An improved whale optimization algorithm based PIDF-(1+PI) cascade automatic generation control for multi-area multi-source power system with capacitive energy storage," *IEEE Access*, vol. 11, pp. 72418–72435, 2023.

[14] M. Raju, L. C. Saikia, and N. Sinha, "Automatic generation control of a multi-area system using ant lion optimizer algorithm based PID plus second order derivative controller," *Int. J. Electr. Power Energy Syst.*, vol. 80, pp. 52–63, Sep. 2016.

[15] J. Morsali, K. Zare, and M. Tarafdar Hagh, "Comparative performance evaluation of fractional order controllers in LFC of two-area diverse-unit power system with considering GDB and GRC effects," *J. Electr. Syst. Inf. Technol.*, vol. 5, no. 3, pp. 708–722, Dec. 2018.

[16] S. Oladipo, Y. Sun, and Z. Wang, "Application of a new fusion of flower pollinated with pathfinder algorithm for AGC of multi-source interconnected power system," *IEEE Access*, vol. 9, pp. 94149–94168, 2021.

[17] B. Cavdar, E. Sahin, E. Sesli, O. Akyazi, and F. M. Nuroglu, "Cascaded fractional order automatic generation control of a PV-reheat thermal power system under a comprehensive nonlinearity effect and cyber-attack," *Electr. Eng.*, vol. 105, no. 6, pp. 4339–4360, Dec. 2023.

[18] E. Çelik, "Design of new fractional order PI-fractional order PD cascade controller through dragonfly search algorithm for advanced load frequency control of power systems," *Soft Comput.*, vol. 25, no. 2, pp. 1193–1217, Jan. 2021.

[19] S. Xie, Y. Zeng, J. Qian, F. Yang, and Y. Li, "CPSOGSA optimization algorithm driven cascaded 3DOF-FOPID-FOPI controller for load frequency control of DFIG-containing interconnected power system," *Energies*, vol. 16, no. 3, p. 1364, Jan. 2023.

[20] S. K. Bhagat, L. C. Saikia, and N. R. Babu, "Application of artificial hummingbird algorithm in a renewable energy source integrated multi-area power system considering fuzzy based tilt integral derivative controller," *e-Prime Adv. Electr. Eng., Electron. Energy*, vol. 4, Jun. 2023, Art. no. 100153.

[21] A. R. Meena and S. S. Kumar, "Genetically tuned fuzzy PID controller in two area reheat thermal power system," *Russian Electr. Eng.*, vol. 87, no. 10, pp. 579–587, Oct. 2016.
[22] B. P. Sahoo and S. Panda, "Improved grey wolf optimization technique for fuzzy aided PID controller design for power system frequency control," *Sustain. Energy, Grids Netw.*, vol. 16, pp. 278–299, Dec. 2018.
[23] J. Liu, "Optimal design of frequency load control system in multi-zone power system using PID-fuzzy controller optimized by bee algorithm," *Multiscale Multidisciplinary Model., Experiments Design*, vol. 6, no. 2, pp. 291–303, Jun. 2023.
[24] O. A. Am, H. Wang, and Y. Tian, "Enhanced model-free discrete-time adaptive terminal sliding-mode control for SOFC power plant with input constraints," *Arabian J. Sci. Eng.*, vol. 47, no. 3, pp. 2851–2864, Mar. 2022.
[25] A. M. O. Abbaker, H. Wang, and Y. Tian, "Adaptive integral type-terminal sliding mode control for PEMFC air supply system using time delay estimation algorithm," *Asian J. Control*, vol. 24, no. 1, pp. 217–226, Jan. 2022.
[26] C.-S. Chiu, "Derivative and integral terminal sliding mode control for a class of MIMO nonlinear systems," *Automatica*, vol. 48, no. 2, pp. 316–326, Feb. 2012.
[27] B. V. Prasanth and S. J. Kumar, "Load frequency control for a two area interconnected power system using robust genetic algorithm controller," *J. Theor. Appl. Inf. Technol.*, vol. 4, no. 12, pp. 1204–1212, 2008.
[28] B. Mohanty, "TLBO optimized sliding mode controller for multi-area multi-source nonlinear interconnected AGC system," *Int. J. Electr. Power Energy Syst.*, vol. 73, pp. 872–881, Dec. 2015.
[29] G. I. Y. Mustafa, H. Wang, and Y. Tian, "Model-free adaptive fuzzy logic control for a half-car active suspension system," *Stud. Informat. Control*, vol. 28, no. 1, pp. 13–24, Mar. 2019.
[30] M. Haddar, M. Bouslema, S. C. Baslamisli, F. Chaari, and M. Haddar, "Improving the ride comfort of full car model with a decoupling intelligent model free controller," *Proc. Inst. Mech. Eng., D, J. Automobile Eng.*, vol. 237, no. 13, pp. 3214–3231, Nov. 2023.
[31] G. P. das Neves and B. A. Angélico, "Model-free control of mechatronic systems based on algebraic estimation," *Asian J. Control*, vol. 24, no. 4, pp. 1575–1584, Jul. 2022.
[32] H. P. Wang, G. I. Y. Mustafa, and Y. Tian, "Model-free fractional-order sliding mode control for an active vehicle suspension system," *Adv. Eng. Softw.*, vol. 115, pp. 452–461, Jan. 2018.
[33] A. O. Abbaker, H. Wang, and Y. Tian, "Voltage control of solid oxide fuel cell power plant based on intelligent proportional integral-adaptive sliding mode control with anti-windup compensator," *Trans. Inst. Meas. Control*, vol. 42, no. 1, pp. 116–130, Jan. 2020.
[34] H. Wang, H. Xu, Y. Tian, and H. Tang, "α-variable adaptive model free control of iReHave upper-limb exoskeleton," *Adv. Eng. Softw.*, vol. 148, Oct. 2020, Art. no. 102872.
[35] U. M. Al-Saggaf, R. Mansouri, M. Bettayeb, I. M. Mehedi, and K. Munawar, "Robustness improvement of the fractional-order LADRC scheme for integer high-order system," *IEEE Trans. Ind. Electron.*, vol. 68, no. 9, pp. 8572–8581, Sep. 2021.
[36] M. Khamies, G. Magdy, M. E. Hussein, F. A. Banakhr, and S. Kamel, "An efficient control strategy for enhancing frequency stability of multi-area power system considering high wind energy penetration," *IEEE Access*, vol. 8, pp. 140062–140078, 2020.
[37] G. Magdy, E. A. Mohamed, G. Shabib, A. A. Elbaset, and Y. Mitani, "SMES based a new PID controller for frequency stability of a real hybrid power system considering high wind power penetration," *IET Renew. Power Gener.*, vol. 12, no. 11, pp. 1304–1313, Aug. 2018.
[38] S. C. Tripathy, R. Balasubramanian, and P. S. C. Nair, "Effect of superconducting magnetic energy storage on automatic generation control considering governor deadband and boiler dynamics," *IEEE Trans. Power Syst.*, vol. 7, no. 3, pp. 1266–1273, Aug. 1992.
[39] J. Morsali, K. Zare, and M. T. Hagh, "Appropriate generation rate constraint (GRC) modeling method for reheat thermal units to obtain optimal load frequency controller (LFC)," in *Proc. 5th Conf. Thermal Power Plants (CTPP)*, Jun. 2014, pp. 29–34.
[40] E. B. Shahrodi and A. Morched, "Dynamic behaviour of AGC systems including the effects of nonlinearities," *IEEE Trans. Power App. Syst.*, vol. PAS-104, no. 12, pp. 3409–3415, Dec. 1985.
[41] A. Levant, "Universal single-input-single-output (SISO) sliding-mode controllers with finite-time convergence," *IEEE Trans. Autom. Control*, vol. 46, no. 9, pp. 1447–1451, Sep. 2001.
[42] A. Levant, "Robust exact differentiation via sliding mode technique," *Automatica*, vol. 34, no. 3, pp. 379–384, Mar. 1998.
[43] J. A. Moreno and M. Osorio, "Strict Lyapunov functions for the super-twisting algorithm," *IEEE Trans. Autom. Control*, vol. 57, no. 4, pp. 1035–1040, Apr. 2012.
[44] M. P. Aghababa, S. Khanmohammadi, and G. Alizadeh, "Finite-time synchronization of two different chaotic systems with unknown parameters via sliding mode technique," *Appl. Math. Model.*, vol. 35, no. 6, pp. 3080–3091, Jun. 2011.
[45] Y. Wang, G. Luo, L. Gu, and X. Li, "Fractional-order nonsingular terminal sliding mode control of hydraulic manipulators using time delay estimation," *J. Vib. Control*, vol. 22, no. 19, pp. 3998–4011, Nov. 2016.

OMER ABBAKER AHMED MOHAMMED received the B.Sc. degree in electrical and electronic engineering from Nyala University, Nyala, Sudan, in 2013, the M.Sc. degree in control engineering from Karary University, Khartoum, Sudan, in 2016, and the Ph.D. degree in control science and engineering from Nanjing University of Science and Technology, China, in 2022. He is currently a Postdoctoral Researcher with the School of Mechanical and Electrical Engineering, Guangzhou University. His current research interests include the theory and applications of model-free control, sliding mode control, fuzzy logic systems, observation design, load frequency control, and modeling and control of fuel cells systems.

LINGXI PENG received the Ph.D. degree in computer application technology from Sichuan University, China, in 2008. He is currently a Professor with the School of Mechanical and Electrical Engineering, Guangzhou University. His current research interests include artificial intelligence and image processing.

GEHAD ABDULLAH AMRAN received the B.S. degree in information technology from Thamar University, Yemen, and the M.Sc. degree in software engineering from Northeastern University. He is currently pursuing the Ph.D. degree in management science and engineering with Dalian University of Technology, China. He was with NEUSOFT Corporation, Shenyang, China, as an Research and Development Engineer. He has authored or coauthored more than 20 journal and conference papers in well-reputed international journals. His research interests include data mining, artificial intelligence, computational intelligence and optimization algorithms, networking, blockchain IoT, recommender systems, and deep neuroevolutionary.

HUSSAIN ALSALMAN received the B.Sc. and M.Sc. degrees in computer science from King Saud University (KSU), Riyadh, Saudi Arabia, and the Ph.D. degree in artificial intelligence from U.K. He is a Staff Member with the Computer Science Department, KSU. He worked for several years as a consultant for several companies in the private sector and institutes in the government sector in Saudi Arabia. From 2009 to 2014, he chaired the Computer Science Department, College of Computer and Information Sciences, KSU. His main research interests include medical image processing, machine learning algorithms, neural networks, computational methods for health care monitoring, and ensemble and deep learning models for medical analysis and diagnosis. He was a member of the review board of the *Saudi Computer Journal*, from 2004 to 2014.

MODAWY ADAM ALI ABDALLA (Member, IEEE) received the B.Sc. degree in electrical and electronics engineering from Nyala University, Nyala, Sudan, in 2012, the M.Sc. degree in electrical engineering from Sudan University of Science and Technology, Khartoum, Sudan, in 2015, and the Ph.D. degree in electrical engineering from Hohai University, Nanjing, China, in 2023. He is currently an Assistant Professor with the Department of Electrical and Electronics Engineering, Nyala University. His current research interests include power systems optimization, demand side management, renewable energies, electric vehicles, smart homes, and smart grids. He received the Jiangsu Provincial Government Scholarship for Outstanding International Students, Hohai University, Nanjing, China, in December 2021. He is currently serving as a Reviewer for the *Journal of Engineering Research* (Elsevier), *Energies* (MDPI), IEEE ACCESS (IEEE), and *Electrical Engineering and Journal of Cleaner Production*.

OMAR ALKAWMANI received the B.Sc. degree in electronic information and telecommunication engineering from Northeastern University, China, where he is currently pursuing the master's degree in electronic information and telecommunication engineering. His research interests include cyber security, wireless sensor networks, and the Internet of Things.

MUHAMMAD MURSIL received the B.Sc. degree in software engineering from Riphah International University, Pakistan, and the master's degree in software engineering from Northeastern University, China. He was with NEUSOFT Corporation, Shenyang, China, as a Research and Development Engineer. He is currently is a Predoctoral Researcher affiliated with the Intelligent Robotics and Computer Vision Group, Department of Computer Science and Mathematics, University of Rovira i Virgili, Tarragona, Spain. His research interests include artificial intelligence, machine learning, and deep learning, with the application of these technologies in different walks of life, especially in the field of medical.

BASSIOUNY SALEH received the Ph.D. degree in engineering mechanics from the College of Mechanics and Materials, Hohai University (HHU), Nanjing, China, in 2021. With over ten years of research experience in material science and technology, he has gained extensive expertise in the field. Currently, he has been holds the position of Postdoctoral Researcher with the College of Energy and Power Engineering, Nanjing University of Aeronautics and Astronautics, since June 2023. He has published over 70 peer-reviewed journal articles and conference articles in the field of metallurgy and materials science. He actively contributes to the global research community and serves as a reviewer for various manufacturing and materials journals. His current research interests include functionally graded materials, metal matrix composites, additive manufacturing, severe plastic deformation, high entropy alloys, wear, casting, and corrosion analysis.